Detectability of QCD phase transitions in binary neutron star mergers: Bayesian inference with the next generation gravitational wave detectors

Aviral Prakash,[1,2] Ish Gupta,[1,2] Matteo Breschi,[3,4,5] Rahul Kashyap,[1,2] David Radice,[1,2,6] Sebastiano Bernuzzi,[3] Domenico Logoteta,[7,8] and B. S. Sathyaprakash[1,2,6]

[1]*Institute for Gravitation and the Cosmos, The Pennsylvania State University, University Park, Pennsylvania 16802, USA*
[2]*Department of Physics, The Pennsylvania State University, University Park, Pennsylvania 16802, USA*
[3]*Theoretisch-Physikalisches Institut, Friedrich-Schiller-Universität Jena, 07743 Jena, Germany*
[4]*Scuola Internazionale Superiore di Studi Avanzati (SISSA), 34136 Trieste, Italy*
[5]*Istituto Nazionale di Fisica Nucleare (INFN), Sezione di Trieste, 34127 Trieste, Italy*
[6]*Department of Astronomy and Astrophysics, The Pennsylvania State University, University Park, Pennsylvania 16802, USA*
[7]*Dipartimento di Fisica, Università di Pisa, Largo B. Pontecorvo, 3 I-56127 Pisa, Italy*
[8]*INFN, Sezione di Pisa, Largo B. Pontecorvo, 3 I-56127 Pisa, Italy*

(Received 27 October 2023; accepted 14 February 2024; published 6 May 2024)

We study the detectability of postmerger QCD phase transitions in neutron star binaries with next-generation gravitational-wave detectors Cosmic Explorer and Einstein Telescope. We perform numerical relativity simulations of neutron star mergers with equations of state that include a quark deconfinement phase transition through either a Gibbs or Maxwell construction. These are followed by Bayesian parameter estimation of the associated gravitational-wave signals using the NRPMw waveform model, with priors inferred from the analysis of the inspiral signal. We assess the ability of the model to measure the postmerger peak frequency $f_2^{\rm peak}$ and identify aspects that should be improved in the model. We show that, even at postmerger signal to noise ratios as low as 10, the model can distinguish (at the 90% level) $f_2^{\rm peak}$ between binaries with and without a phase transition in most cases. Phase-transition induced deviations in the $f_2^{\rm peak}$ from the predictions of equation-of-state insensitive relations can also be detected if they exceed 1.6σ. Our results suggest that next-generation gravitational wave detectors can measure phase transition effects in binary neutron star mergers. However, unless the phase transition is "strong," disentangling it from other hadronic physics uncertainties will require significant theory improvements.

DOI: 10.1103/PhysRevD.109.103008

I. INTRODUCTION

The discoveries of the gravitational wave (GW) event GW170817 [1] from a merger of two neutron stars, the associated short gamma ray burst GRB170817A and the optical transient AT2017gfo [2], revitalized the field of multimessenger astronomy. It is now possible to probe high-energy astrophysical phenomena through their GW signatures in addition to electromagnetic radiation. The emitted GW spectra from a merger of two neutron stars spans a broad range of frequencies. GWs from an inspiral (at frequencies $\lesssim 10^3$ Hz) signal provide a wealth of information about the intrinsic properties of a binary such as its component masses and tidal deformabilities. On the other hand, postmerger GW emission (at frequencies $\gtrsim 10^3$ Hz) can inform us about the dynamically evolving merger remnant. No postmerger signal from GW170817 was detected thereby leaving to speculation the fate of the remnant. We encourage the reader to refer to Refs. [3,4] for recent reviews.

With the upcoming generation of GW detectors like the Einstein Telescope (ET) [5,6] or the Cosmic Explorer (CE) [7–10], it is expected that the postmerger phase of evolution will be within reach of detector sensitivities [11,12]. This would imply observational constraints on the physical processes in neutron star mergers, particularly the ones arising in the postmerger. The postmerger emission is characterized by GWs emitted in the kilohertz regime from the dynamically ($\mathcal{O} \sim 10^{-3}$ s) changing quadrupolar moment of the merger remnant. Changes in the quadrupolar moment depend strongly on the underlying equation of state (EOS) which describes the thermodynamic equilibrium state of matter in the neutron star bulk. EOSs may involve a multitude of physical processes like temperature dependent effects [13–17], neutrino interactions and microphysics [18–36], appearance of hyperons [37,38], and high-density phase transitions [15,37–55] which can leave imprints on the postmerger emission. Additionally, magnetic fields and magnetohydrodynamic turbulence [56–60]

may influence the postmerger emission by redistributing the angular momentum in the remnant.

In recent years, there has been a significant impetus in understanding the behavior of supranuclear ($>2.7 \times 10^{14}$ g cm^{-3}) matter expected to be realized in and around the core of heavy neutron stars, neutron star merger remnants or core collapse supernovae. Processes like a possible phase transition to deconfined quark matter or the appearance of hyperons have garnered particular interest in reference to binary neutron star (BNS) mergers as they are expected to influence the postmerger GW emission from a merger remnant which in turn can provide excellent test beds for probing strongly interacting matter. Modeling efforts in this direction typically involve comparing GW emission from a nucleonic EOS to that computed from an EOS that has additional degrees of freedom. In this regard, the works by Sekiguchi *et al.* [37] and Radice *et al.* [38] explored the appearance of hyperons in a BNS merger and reported on their effects on the postmerger GW signal, i.e., a compactification of the merger remnant leading to shorter postmerger signals as compared to models without hyperons.

Most *et al.* [39,40] considered a first order phase transition to deconfined quarks and obtained similar results for the postmerger GW emission along with a small dephasing. The works by Bauswein *et al.* [41,42] identified large shifts (30–121 Hz) in the postmerger peak frequency (which we call $f_2^{\rm peak}$ in this work) of their quark models as compared to their hadronic models. They claimed that sufficiently large shifts in $f_2^{\rm peak}$, breaking the degeneracy of EOS-insensitive relations, could be a telltale sign of first order phase transitions. Extending this work, Blacker *et al.* [43] attempted to constrain the onset density of such phase transitions. In another work Blacker *et al.* [15] disentangled and explored the thermodynamics of deconfined quark matter with respect to BNS mergers. Weih *et al.* [44] reported on double-peaked frequency spectra as a signature of a delayed phase transition that resulted in a metastable hypermassive neutron star (HMNS). Studies by Prakash *et al.* [45] however, found no smoking-gun evidences of GW signatures and observed shifts in postmerger peak frequency that were degenerate with other hadronic EOSs. They also computed potential electromagnetic signatures of these phase transitions. Liebling *et al.* [46] computed similar postmerger GW signatures and observed changes in the magnetic field topology in the bulk of the star. In contrast to modeling first-order phase transitions, Refs. [47–49] explored such deconfinement processes via a quark-hadron crossover (QHC) by constraining the $f_2^{\rm peak}$ and chirp frequencies. In this regard, Fujimoto *et al.* [50] have compared GW signatures arising from a first-order phase transition with those from a QHC and show the results from the QHC scenario to be consistent with electromagnetic counterparts observed from GW170817.

More recently, there have been efforts [51,52] to employ the novel holographic V-QCD framework to construct EOSs with a deconfinement phase transition and compute their GW signals. Consistent with previous works, an early collapse for softer EOSs is observed. Espino *et al.* [53], for the first time, investigated multimodal signatures of deconfinement phase transitions and reported on a weakening of the one-armed spiral instability that increased with the strength of the phase transition. Guo *et al.* [54] contrasted the GW signatures between EOSs that modeled such phase transitions via a Maxwell's construction, a Gibb's construction and a QHC and showed that lower phase transition densities lead to more compact remnants that collapse into a black hole. In a parallel study, Haque *et al.* [55] varied the onset density of the phase transition and examined its impact on the postmerger GW frequency.

Both premerger (late inspiral) and postmerger phases of a BNS evolution can provide useful information with reference to phase transitions to deconfined quarks. Extensive efforts by several groups have gone into modeling the postmerger GW emission [61–68]. Chatziioannou *et al.* [69] and Wijngaarden *et al.* [70] employ model independent inference via BayesWave to resconstruct the postmerger signals while using NR calibrated compact binary coalescence templates for the inspiral. While this kind of a hybrid model-agnostic approach does indeed offer more flexibility towards modeling particular waveform morphologies as compared to analytical models, an absence of a model implies no way for a likelihood computation and hence a comparison using Bayes' factors or odd's ratios to other approaches cannot be made. On the other hand, Easter *et al.* [64] and Tsang *et al.* [66] employed damped sinusoidal models to describe the postmerger emission. Breschi *et al.* [67,68] constructed analytic models of postmerger emission that were calibrated by numerical relativity (NR) simulations. Subsequently, these models were employed in Refs. [67,71,72] to potentially detect EOS softening via the production of Λ hyperons. In particular, Breschi *et al.* [71] recovered differences in the postmerger peak frequency and remnant lifetimes to constrain the said effects in a BNS merger. In yet another recent work, Harada *et al.* [73] employ Bayesian model selection to distinguish between models that respectively include and exclude a smooth crossover to a deconfined quark phase during the postmerger evolution.

To complement the above mentioned postmerger studies, there have also been several efforts to constrain nuclear properties of high-density matter using the late inspiral phase of a binary merger [69,74–77]. In particular, Mondal *et al.* [78] employed a phenomenological metamodeling approach to the EOSs and constrained QCD phase transitions via measurements of tidal parameters. Essick *et al.* [77] constructed nonparametric representations of EOSs and attempted to infer an onset of QCD phase transitions from the EOS itself. Raithel *et al.* [76] have examined the

impact of phase transition on an inference of tidal deformability using inspiral GW signals and have found degeneracies between the EOS with phase transition and that with hadrons while keeping the tidal deformability constant. Raithel *et al.* [79] also present an interesting case of "tidal deformability doppelgängers" where they employ quark EOSs with differences in pressure at nuclear saturation but which predict tidal parameters consistent with that of exclusively hadronic EOSs. Pang *et al.* [80] have computed Bayes factors of binary mergers with and without a phase transition while also considering the strength of phase transitions as a parameter for Bayesian inference.

While most of the works discussed above remark that such deconfinement phase transitions (and EOS softening effects in general) are potentially detectable, the Refs. [49,62,64,67,70–72,77,78,80] pave a concrete path in defining an observational strategy to observe their effects with kilohertz gravitational waves.

It has been shown from NR simulations of neutron star binaries [46,61,81–87] that there exists a correlation between the $f_2^{\rm peak}$ frequency of the postmerger and an inspiral property of the binary, e.g., a suitable combination of tidal parameters from the inspiral, the radius of a neutron star of a fixed mass or the compactness of a neutron star. Such relations are insensitive to the EOS and are also referred to as quasiuniversal relations (QURs). Indeed, such relations have been employed to construct analytical waveform models [67,68]. Several works [41,42] claim that a violation of a universal relation between $f_2^{\rm peak}$ and the tidal deformability of a $1.35M_\odot$ neutron star ($\Lambda_{1.35}$) can be taken to be a smoking-gun evidence of QCD phase transitions. Wijngaarden *et al.* [70] even demonstrate that Bayesian error estimates for a joint detection of $f_2^{\rm peak}$ and $\tilde{\Lambda}$ at sufficiently high signal-to-noise ratios (SNRs) can be distinguished from the established QURs. At the same time, Breschi *et al.* in Ref. [72] perform a pre/postmerger consistency test and show that a breaking of an EOS insensitive relation between $f_2^{\rm peak}$ and tidal polarizability κ_2^T to a given confidence level cannot be taken to be a confident signature of the softening of the EOS. In this work, we place our calculations in the context of previous findings by applying error estimates from Bayesian inference to NR simulations.

We utilize Bayesian inference on the inspiral and postmerger signals to recover estimates on tidal properties and postmerger spectra, respectively. We then use these estimates in reference to the universal relation by Breschi *et al.* [68] to show a potential detectability of QCD phase transitions at postmerger SNRs as low as 10. To this aim, we employ composition-dependent, finite-temperature EOSs describing the high-density behavior of strongly interacting matter and compute the postmerger GW emission of a BNS merger remnant. We employ the frequency domain waveform model NRPMw developed by Breschi *et al.* [68] to recover the spectra of the said NR waveforms assuming sensitivities of the next generation GW detectors. This paper is organized as follows: in Sec. II A, we describe the NR simulations used in this work. In Sec. II B, we comment upon the procedure employed to create postmerger injections from our NR dataset. Following this in Sec. II C, we briefly recapitulate the methodology for Bayesian inference of parameters given an analytic BNS waveform model. Finally in Sec. II D, we describe two choices of priors employed in our work which are respectively informed and agnostic of the inspiral signal. We present our results in Sec. III where we classify our (postmerger) parameter estimation (PE) analysis in two categories with different choices of priors. Primarily in Sec. III A, we take inspiral-informed Gaussian priors on masses and tidal parameters for the postmerger. Secondarily, we present a test case in Appendix A wherein we assume broad priors for the postmerger model NRPMw's parameters and perform an inspiral-agnostic PE. In Sec. III B, we repeat the postmerger analysis with the CE detectors: the broad-band CE-40 and the narrow-band postmerger optimized CE-20. In Sec. III C, we use an NR informed EOS insensitive relation to probe phase transitions at a given postmerger SNR. Finally, we conclude the paper in Sec. IV. In the Appendices, we provide results for all our simulations as well as a miscellany of supplemental results. In Appendices A and B, we provide results for the entire simulation dataset. Finally, in Appendix C, we provide results from a flexible configuration of the NRPMw model aimed at addressing some of the biases encountered in recovering hadronic models.

II. METHODS

A. NR simulations

We summarize the NR simulations used in this work in Table I. Our dataset primarily consists of BNS merger simulations with hadronic and quark EOSs presented in Ref. [45]. We also perform merger simulations with two additional EOSs DD2F [88,89] and DD2F-SF1 [41,90] to include effects from different treatments of strongly interacting matter. The mergers we consider produce remnants that do not collapse promptly and result in a finite postmerger GW signal (see Table I). We employ the numerical infrastructure in Ref. [45] and references therein for all our NR simulations. In particular, we solve the equations of general relativistic hydrodynamics (GRHD) in the $3+1$ Valencia Formulation [91] using the publicly available code WhiskyTHC [92–94]. We employ the CTGamma [95,96] code available as part of the Einstein Toolkit [97] to solve for the spacetime in the Z4c formulation [98,99] of the Einstein's equations. We use the WeylScal4 and Multipole thorns to compute the spin $s=-2$ weighted spherical harmonics of the Newman-Penrose scalar Ψ_4, from which we extract the GW strain of the $\ell=2$, $m=2$ mode. Additionally, we employ a zeroth moment M0 scheme [18]

TABLE I. A summary of NR simulations employed in this work. The corresponding postmerger waveforms are used in the construction of injections for the next generation GW detectors and for the subsequent Bayesian inference. EOS represents the equation of state, m_1 and m_2 the gravitational masses of the binary ($m_1 > m_2$), q the mass ratio, Λ_is the tidal deformabilities and $t_{\rm BH}$ the time of black hole formation expressed relative to the time of merger $t_{\rm merg}$. The acronym HMNS represents a hypermassive neutron star remnant that does not collapse within the simulation timescale.

EOS	$m_1\,[M_\odot]$	$m_2\,[M_\odot]$	q	Λ_1	Λ_2	$t_{\rm BH} - t_{\rm merg}$ [ms]
BLh	1.298	1.298	1.0	701.901	701.901	HMNS
BLQ	1.298	1.298	1.0	701.901	701.901	15.95
BLh	1.481	1.257	1.178	295.467	856.064	HMNS
BLQ	1.481	1.257	1.178	295.467	856.064	3.54
BLh	1.398	1.198	1.167	435.735	1145.850	HMNS
BLQ	1.398	1.198	1.167	435.735	1145.850	17.2
BLh	1.363	1.363	1.0	515.379	515.379	HMNS
BLQ	1.363	1.363	1.0	515.379	515.379	4.1
DD2F	1.289	1.289	1.0	707.511	707.511	HMNS
DD2F-SF1	1.289	1.289	1.0	707.511	707.511	42.36

to solve for the neutrino energies and neutrino number densities. We construct initial data assuming irrotational binaries in quasicircular orbits using the pseudospectral code Lorene [100]. The binaries are situated at an initial separation of 45 km ($30.47\,M_\odot$). Finally, we employ the Carpet [101,102] code for providing the adaptive mesh refinement infrastructure.

To probe multiple possibilities in the high-density regime of QCD, we take a selection of four finite-temperature EOSs namely BLh [103,104], DD2F [88,89], BLQ [45,71,105,106], and DD2F-SF1 [41,90]. For these EOSs, the pressure-density curves at 0 temperature are shown in Fig. 1. Of these, the BLh and DD2F EOSs contain only nucleonic degrees of freedom whereas the BLQ and DD2F-SF1 EOSs implement a first order phase transition to deconfined quark matter while having the same low-density behavior as the BLh and DD2F EOSs, respectively. The BLQ EOS employs a Gibbs construction to combine the hadronic and quark phases resulting in a mixed phase of deconfined quarks and hadrons. There is a gradual increase in the percentage of deconfined quarks with nonzero temperatures and densities $\gtrsim 3\rho_{\rm nuc}$ where

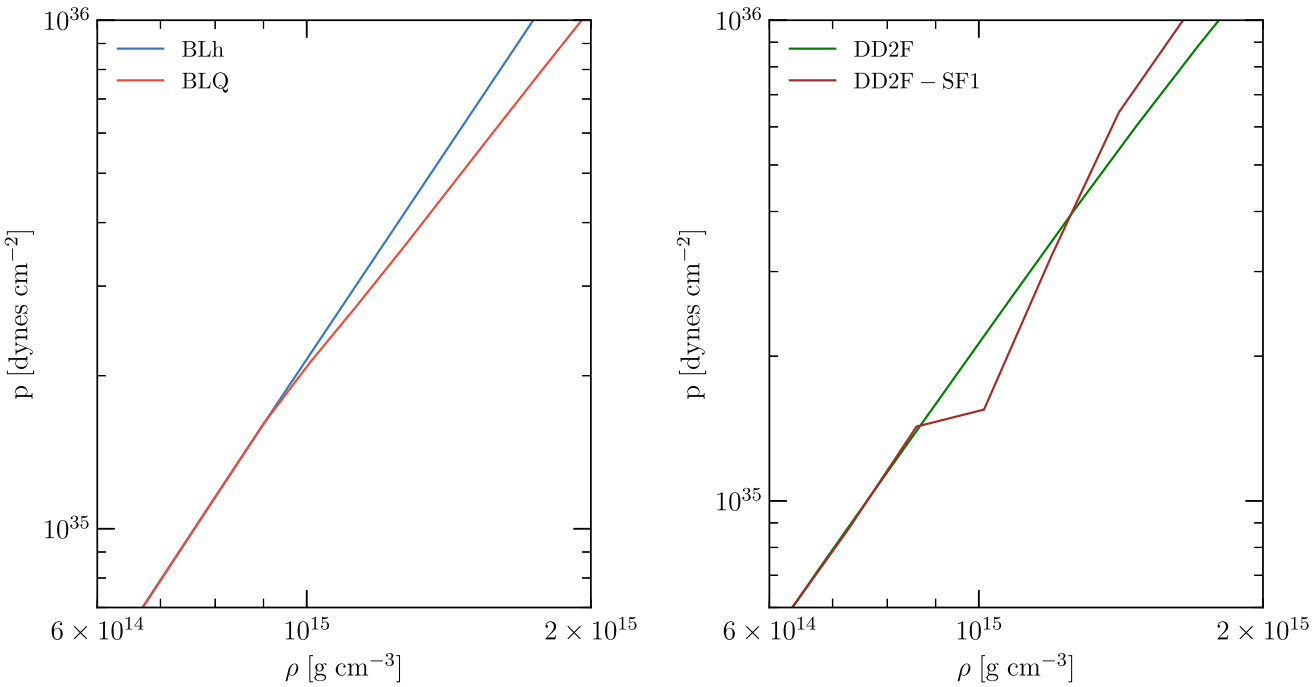

FIG. 1. Pressure-density curves for the $T = 0$ (zero temperature) slice of the EOSs used in this work. BLh and DD2F EOSs contain only nucleonic degrees of freedom whereas BLQ and DD2F-SF1 also include a prescription for a first-order phase transition to deconfined quarks. Such a phase transition leads to a loss of pressure at high densities $\rho \sim 10^{15}$ g cm^{-3}.

$\rho_{\rm nuc} = 2.7 \times 10^{14}$ g cm^{-3} is the nuclear saturation density. The DD2F-SF1 EOS on the other hand employs a Maxwell construction that allows for a less gradual transition to the deconfined quark phase as compared to the BLQ EOS.

As previously found in Bauswein *et al.* [41], the BNS models evolved with the DD2F-SF family of EOSs display large deviations from the EOS insensitive relation between the postmerger peak frequency $f_2^{\rm peak}$ and tidal deformability Λ. On the other hand, models with the BLQ EOS [45] predict postmerger peak frequencies that are within range of those spanned by hadronic EOSs and obey the $f_2^{\rm peak} - \kappa_2^T$ relation obtained in Ref. [67] where κ_2^T is the tidal polarizability defined in the same reference. It is important to emphasize that the EOS insensitive relation obtained and the simulation setup employed in Ref. [41] is not the same as the one used in Ref. [67]. Therefore, for consistent comparison, we performed simulations with the DD2F-SF1 EOS with our GRHD infrastructure and find that models with this EOS also display large deviations with the $f_2^{\rm peak} - \kappa_2^T$ relation. We also note that the simulations presented in our work are computed in full general relativity (GR) whereas the ones from Bauswein *et al.* [41] consider a conformal flatness condition to solve for the Einstein's equations.

Additionally, we consider unequal mass mergers for the BLh and BLQ EOSs to account for the impact of mass ratios. With this diversity in the choice of EOSs and the masses of BNS mergers, our study provides reasonable estimates of the GW detectability of QCD phase transitions in BNS mergers. In addition to that, we would like to remark here that even though the waveform model NRPMw is trained on a large number of NR simulations spanning 21 EOSs, simulations with DD2F and DD2F-SF1 EOSs have not been utilized for training the model and therefore validate the model's performance.

B. Injection settings

In this section, we describe the procedure for constructing postmerger injections from our NR simulations for a Bayesian inference study. In particular, we scale the GW strain obtained from NR simulations and introduce it in a data stream which serves to simulate the incoming GW in a detector. To compute the $\ell = 2, m = 2$ GW strain output from the NR simulations, we first evaluate the Newman-Penrose scalar Ψ_4 on coordinate spheres in a multipolar spherical harmonic basis. This scalar (for the $\ell = 2, m = 2$ mode) is then integrated twice in time using fixed frequency integration [107] to obtain the quadrupolar strain h_+ and $h_\times$. Fixed frequency integration also helps remove secular drifts in the strain amplitude that may arise because of direct integration of Ψ_4.

We define the time of merger $t_{\rm merg}$ as the time when the GW amplitude of the $\ell = 2$, $m = 2$ mode, i.e., $(h_+^2 + h_\times^2)^{1/2}$ is maximum. We construct the injections by considering only the postmerger portion of the NR waveform starting from $t_{\rm merg}$ up until the termination of the waveform. For the remnants that collapse into a black hole (BH), we define a time of BH formation $t_{\rm BH}$ (Table I) as the time when the minimum value of the lapse function in the computational grid drops below 0.2, which approximately corresponds to the formation of an apparent horizon for remnants resulting from a merger of nonspinning binaries. This definition of the collapse of a remnant has been motivated from Ref. [108] and employed in works like [45,105,109]. We extract the postmerger signal ($t > t_{\rm merg}$) by employing a Tukey window [110] available as part of the SciPy library. In particular, we use a windowing ansatz w of the form

$$w(t, t_0, t_1, \delta) = \begin{cases} 0 & \text{if } t < t_0 \\ \tau(t, \delta) & \text{if } t \in [t_0, t_1], \\ 0 & \text{if } t > t_1 \end{cases} \tag{1}$$

where τ denotes the standard Tukey window of width $|t_1 - t_0|$ and a shape parameter δ that controls the fraction of the window inside the tapered region. Furthermore, we spline interpolate the waveforms to a sampling rate of 16,384 Hz and zero pad them to a signal segment of 1 s, as shown in Fig. 2. To systematically disentangle the effects of QCD phase transitions on the GW strain from the effects of detector noise, we construct noiseless injections. The posteriors on model parameters recovered in such a noiseless configuration approximate the average over those recovered from multiple Gaussian noise realizations.

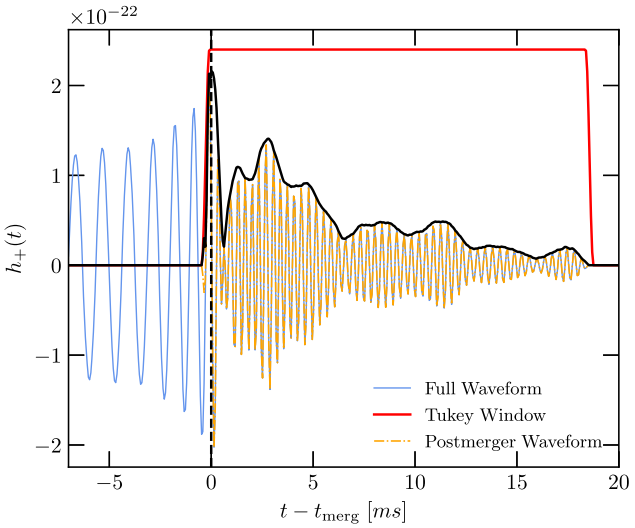

FIG. 2. Extraction of the postmerger waveform from an NR waveform by applying a Tukey window. This windowed waveform upon spline interpolation and zero padding is then injected in a noiseless configuration of the ET/CE detectors for parameter estimation using NRPMw.

Finally, we scale the waveforms by a factor of the inverse luminosity distance D_L^{-1} and the spin $s=-2$ weighted spherical harmonics ${}_{-2}Y_{2,2}(\iota=0,\psi=0)$ for a face-on configuration to consistently maintain a postmerger SNR of 10 in the ET detector network or in the CE-20 detector. This corresponds to placing each BNS system at different luminosity distances with respect to the detector as described in Tables IV and V.

C. Parameter estimation

For our postmerger PE analysis, we employ the nested sampler UltraNest [111] included as part of the BAJES code [112]. Our configuration employs 5×10^3 live points and a maximum of 5×10^4 iterations for the Monte Carlo sampler. We choose a Gaussian-noise likelihood [113] defined as

$$\log\left(\mathcal{L}(d|\boldsymbol{\theta})\right)=-\frac{1}{2}\sum_j\log\left(2\pi S_j\right)-\frac{1}{2}\sum_j\langle d_j-\mu(\boldsymbol{\theta})|d_j-\mu(\boldsymbol{\theta})\rangle, \quad (2)$$

where the summation index j runs over the three arms in the case of the ET detector, S_j denotes the power spectral density (PSD) of the corresponding detector, $\mu(\boldsymbol{\theta})$ is the NRPMw model evaluated for the parameter set $\boldsymbol{\theta}$, and d represents the data stream of the injection. In the case of the CE detector, we fix j to correspond to the narrow-band 20 km postmerger optimized configuration. The inner product $\langle .|.\rangle$ between two signals say $a(f)$ and $b(f)$ in the frequency domain is given by

$$\langle a(f)|b(f)\rangle=4\,\mathrm{Re}\int_{f_{\min}}^{f_{\max}}\frac{a^*(f)b(f)}{S_j(f)}df. \quad (3)$$

The PSDs for the ET and the CE detectors employed by us are the same as those used in Refs. [10–12]. We take $f_{\min}$ and $f_{\max}$ to be 1024 and 8192 Hz, respectively, to include the postmerger domain of the signal.

We take d_j to denote the data stream in each arm of the detector, i.e., $d_j=s_j+n_j$, where s_j and n_j, respectively, denote the signal and noise in the detector. For noiseless injections, d_j is given exclusively by the signal projected onto the individual detectors, i.e.,

$$d_j(f)=\mathrm{F}_{j;+}(\mathrm{R.A.},\mathrm{DEC.},\psi)h_+(f)+\mathrm{F}_{j;\times}(\mathrm{R.A.},\mathrm{DEC.},\psi)h_\times(f), \quad (4)$$

where $\mathrm{F}_{j;+}$ and $\mathrm{F}_{j;\times}$ denote the antenna pattern functions of the jth arm of the ET detector (or a CE-20 detector) and R.A., DEC., and ψ denote the right ascension, declination, and the polarization angle of the binary, respectively. The injected signal corresponds to the strain from NR simulations.

The joint posterior distribution function (PDF) of the posterior samples corresponding to the parameters of the NRPMw model is given by the Bayes' theorem as

$$p(\boldsymbol{\theta}|d)=\frac{\mathcal{L}(d|\boldsymbol{\theta})\pi(\boldsymbol{\theta})}{\mathcal{Z}}, \quad (5)$$

where $\mathcal{Z}$ denotes the marginalized likelihood or the evidence for the data stream and $\pi(\boldsymbol{\theta})$ denotes the prior PDFs for the model parameters. Finally, to compute the individual posteriors (θ_i) of the model parameters, we marginalize the joint PDF over the corresponding parameters to obtain

$$p(\theta_i|d)=\int\left(\prod_{k\neq i}d\theta_k\right)p(\boldsymbol{\theta}|d). \quad (6)$$

In the NRPMw model presented in Breschi *et al.* [68], the postmerger frequency parameter f_2 is decided by a fit to an EOS insensitive relation (see Table I of Ref. [68]) with κ_2^T and accounted for deviations by using the recalibration parameter δf_2. In this work, we will assume f_2 to be an unconstrained parameter over which we can sample in a Bayesian framework. In other words, this means migrating f_2 from the set of $\boldsymbol{\theta}_{\mathrm{fit}}$ to $\boldsymbol{\theta}_{\mathrm{free}}$, where $\boldsymbol{\theta}_{\mathrm{fit}}$ and $\boldsymbol{\theta}_{\mathrm{free}}$ are, respectively, the sets of fitted parameters and free parameters for NRPMw, as defined in Ref. [68]. The motivation behind making f_2 unconstrained lies in the fact that we do not want our results to be informed in any way by the $f_2-\kappa_2^T$ relation. Throughout this work, we will refer to the global maxima in the reconstructed postmerger spectra as f_2^{peak} to avoid confusion with the f_2 parameter of the NRPMw model, which is a carrier frequency evolving linearly with time. We would like to stress that even though f_2^{peak} and f_2 are close numerically, they are not the same quantity. f_2^{peak} is a property of the reconstructed spectra whereas f_2 is a parameter of the NRPMw model. Posteriors on f_2^{peak} are computed from the global postmerger maxima of the reconstructed signal that in turn depends on f_2 and other parameters. In a nutshell, f_2^{peak} is influenced by the choice of f_2 but not the other way around. Throughout this work, we will refer to this updated model with the unconstrained f_2 parameter as NRPMw. For comparison, we have also presented calculations in Sec. III C with the original model of Breschi *et al.* [68] where f_2 is constrained by κ_2^T and we call this model as NRPMw_v1. Finally, to explore a more flexible configuration of the model, we unconstrain not only f_2 but also f_0 which is the parameter for radial oscillation modes. We refer to this version of the model as NRPMw_v2 and describe it in Appendix C.

D. Priors

With the advent of the next generation of GW detectors, it is expected for binaries that are loud enough that their postmergers can be detected, masses and tidal deformabilities will be measured accurately from the inspiral [11,12]. Therefore, the most accurate PE would result from an analysis of the full signal, i.e., inspiral and postmerger. However, performing Bayesian inference on the full signal is computationally expensive. In this work, we therefore adopt a two-fold approach in the sense that we analyze the inspiral and postmerger signals using separate inference codes. From the inspiral inference, we compute posteriors on total gravitational mass M, mass ratio q, and the tidal deformabilities Λ_is, all of which for loud signals are Gaussians to a good approximation. Following this in a separate inference for the postmerger, we constrain the prior bounds of the postmerger model by supplying the Gaussian priors thus obtained. We refer the reader to Sec. II D 1 for the detailed procedure to compute these priors.

On the other hand, in Sec. II D 2, we describe a choice of priors that are broad and independent of the inspiral signal. We have summarized the two choices of priors in Tables II and III.

TABLE II. Prior ranges for the parameters of the NRPMw model as well as the extrinsic and intrinsic parameters in an inspiral agnostic setting. In particular, the priors on M and q have been set in accordance to Ref. [114] so as to maintain a uniform distribution in m_1 and m_2.

Parameter	Min	Max	Type
M $[M_\odot]$	1	6	Reference [114]
q	1	2	Reference [114]
χ_1	−0.2	0.2	Aligned spin
χ_2	−0.2	0.2	Aligned spin
Λ_1	0	4000	Uniform
Λ_2	0	4000	Uniform
R.A.	0	2π	Uniform
DEC.	$-\pi/2$	$\pi/2$	Cosinusoidal
$\cos\iota$	−1	1	Uniform
ψ	0	π	Uniform
D_L [Mpc]	5	500	Volumetric
$t_{\rm coll}/M$	1	3000	Uniform
$M^2\alpha_{\rm peak}$	-10^{-4}	10^{-4}	Uniform
$\phi_{\rm PM}$	0	2π	Uniform
f_2 [kHz]	1.5	5	Uniform
$\delta(Mf_0)$	−1	2	$\text{Gaussian}^{\mu=0}_{\sigma=0.449}$
$\delta(Mf_{\rm mrg}/\nu)$	−0.2	0.2	$\text{Gaussian}^{\mu=0}_{\sigma=0.026}$
$\delta(A_{\rm mrg}/M)$	−0.2	0.2	$\text{Gaussian}^{\mu=0}_{\sigma=0.018}$
$\delta(M/t_0)$	−0.5	0.5	$\text{Gaussian}^{\mu=0}_{\sigma=0.092}$
$\delta(A_0/M)$	−1	4	$\text{Gaussian}^{\mu=0}_{\sigma=0.663}$
$\delta(A_1/M)$	−1	2	$\text{Gaussian}^{\mu=0}_{\sigma=0.152}$
$\delta(A_2/M)$	−1	2	$\text{Gaussian}^{\mu=0}_{\sigma=0.385}$
$\delta(A_3/M)$	−1	2	$\text{Gaussian}^{\mu=0}_{\sigma=0.269}$
$\delta(M^2\mathcal{I}m(\alpha_{\rm fus})/\nu)$	−4	4	$\text{Gaussian}^{\mu=0}_{\sigma=0.751}$
$\delta(M\mathcal{R}e(\beta_{\rm peak}))$	−1	2	$\text{Gaussian}^{\mu=0}_{\sigma=0.27}$
$\delta(M\Delta_{\rm fm})$	−1	4	$\text{Gaussian}^{\mu=0}_{\sigma=0.744}$
$\delta(M\Gamma_{\rm fm})$	−1	4	$\text{Gaussian}^{\mu=0}_{\sigma=0.977}$

TABLE III. Prior ranges for the parameters of the NRPMw model, the extrinsic and intrinsic parameters in an inspiral informed setting. We constrain priors on M, q, Λ_1, and Λ_2 from the inspiral signal. In this table, we show details for the prior distribution employed for the $1.398M_\odot - 1.198M_\odot$ binary with the BLh EOS. The type of priors remains the same for all models in our work.

Parameter	Min	Max	Type
M $[M_\odot]$	2.641	2.652	$\text{Gaussian}^{\mu=2.646}_{\sigma=0.001}$
q	1.11	1.22	$\text{Gaussian}^{\mu=1.17}_{\sigma=0.01}$
χ_1	−0.2	0.2	Aligned spin
χ_2	−0.2	0.2	Aligned spin
Λ_1	363.94	559.70	$\text{Gaussian}^{\mu=448.24}_{\sigma=18.79}$
Λ_2	1030.17	1203.71	$\text{Gaussian}^{\mu=1123.61}_{\sigma=21.28}$
R.A.	0	2π	Uniform
DEC.	$-\pi/2$	$\pi/2$	Cosinusoidal
$\cos\iota$	−1	1	Uniform
ψ	0	π	Uniform
D_L [Mpc]	5	500	Volumetric
$t_{\rm coll}/M$	1	3000	Uniform
$M^2\alpha_{\rm peak}$	-10^{-4}	10^{-4}	Uniform
$\phi_{\rm PM}$	0	2π	Uniform
f_2 [kHz]	1.5	5	Uniform
$\delta(Mf_0)$	−1	2	$\text{Gaussian}^{\mu=0}_{\sigma=0.449}$
$\delta(Mf_{\rm mrg}/\nu)$	−0.2	0.2	$\text{Gaussian}^{\mu=0}_{\sigma=0.026}$
$\delta(A_{\rm mrg}/M)$	−0.2	0.2	$\text{Gaussian}^{\mu=0}_{\sigma=0.018}$
$\delta(M/t_0)$	−0.5	0.5	$\text{Gaussian}^{\mu=0}_{\sigma=0.092}$
$\delta(A_0/M)$	−1	4	$\text{Gaussian}^{\mu=0}_{\sigma=0.663}$
$\delta(A_1/M)$	−1	2	$\text{Gaussian}^{\mu=0}_{\sigma=0.152}$
$\delta(A_2/M)$	−1	2	$\text{Gaussian}^{\mu=0}_{\sigma=0.385}$
$\delta(A_3/M)$	−1	2	$\text{Gaussian}^{\mu=0}_{\sigma=0.269}$
$\delta(M^2\mathcal{I}m(\alpha_{\rm fus})/\nu)$	−4	4	$\text{Gaussian}^{\mu=0}_{\sigma=0.751}$
$\delta(M\mathcal{R}e(\beta_{\rm peak}))$	−1	2	$\text{Gaussian}^{\mu=0}_{\sigma=0.27}$
$\delta(M\Delta_{\rm fm})$	−1	4	$\text{Gaussian}^{\mu=0}_{\sigma=0.744}$
$\delta(M\Gamma_{\rm fm})$	−1	4	$\text{Gaussian}^{\mu=0}_{\sigma=0.977}$

TABLE IV. A summary of the properties of postmerger injections corresponding to the NR simulations reported in Table I. In this table we present these properties for the choice of priors that is informed by the inspiral signal as described in Sec. III A. In particular, GW model represents the specific configuration of the NRPMw model utilized for the recovery. We us the NRPMw model in three configurations namely, NRPMw, where the f_2 parameter is unconstrained by the $f_2 - \kappa_2^T$ relation, NRPMw_v1 where the f_2 parameter is constrained by the quasiuniversal relation, and the most flexible NRPMw_v2 configuration where both f_2 and f_0 are unconstrained from their respective quasiuniversal relations. Detector is the GW datector used for the recovery of postmerger injections, $f^{\rm peak}_{2;\rm Injected}$ and $f^{\rm peak}_{2;\rm Recovered}$ are, respectively, the injected and recovered postmerger peak frequencies and D_ℓ is the luminosity distance of the binary from the detector. In the last two columns, we report the postmerger signal to noise ratios of the injected and recovered signals.

Index	EOS	$m_1\,[M_\odot]$	$m_2\,[M_\odot]$	GW Model	Detector	$f^{\rm peak}_{2;\rm Injected}$ [kHz]	$f^{\rm peak}_{2;\rm Recovered}$ [kHz]	D_ℓ [Mpc]	$\rho_{\rm injected}$	$\rho_{\rm recovered}$
1	BLh	1.298	1.298	NRPMw	ET	2.804	$2.842^{+0.041}_{-0.025}$	89.049	10	$8.73^{+1.08}_{-1.62}$
2	BLQ	1.298	1.298	NRPMw	ET	2.927	$2.924^{+0.016}_{-0.025}$	93.474	10	$8.61^{+1.10}_{-1.71}$
3	BLh	1.481	1.257	NRPMw	ET	2.962	$2.948^{+0.016}_{-0.025}$	97.503	10	$8.66^{+1.17}_{-1.49}$
4	BLQ	1.481	1.257	NRPMw	ET	3.143	$3.145^{+0.303}_{-0.106}$	83.434	10	$8.75^{+1.20}_{-1.19}$
5	BLh	1.398	1.198	NRPMw	ET	2.758	$2.825^{+0.082}_{-0.066}$	87.027	10	$7.82^{+0.95}_{-1.22}$
6	BLQ	1.398	1.198	NRPMw	ET	2.955	$2.957^{+0.025}_{-0.033}$	87.500	10	$8.75^{+1.17}_{-1.70}$
7	BLh	1.363	1.363	NRPMw	ET	3.074	$3.055^{+0.033}_{-0.025}$	97.282	10	$7.97^{+1.16}_{-1.66}$
8	BLQ	1.363	1.363	NRPMw	ET	3.197	$3.268^{+0.09}_{-0.066}$	78.449	10	$8.60^{+1.33}_{-1.35}$
9	DD2F	1.289	1.289	NRPMw	ET	2.889	$2.916^{+0.025}_{-0.025}$	93.284	10	$8.56^{+1.13}_{-1.70}$
10	DD2F-SF1	1.289	1.289	NRPMw	ET	3.354	$3.284^{+0.213}_{-0.172}$	78.247	10	$8.53^{+1.25}_{-1.25}$
11	DD2F-SF1	1.289	1.289	NRPMw	ET	3.354	$3.325^{+0.106}_{-0.041}$	52.165	15	$12.34^{+2.17}_{-1.87}$
12	DD2F	1.289	1.289	NRPMw	CE-20	2.888	$2.916^{+0.025}_{-0.025}$	118.467	10	$8.59^{+1.12}_{-2.14}$
13	DD2F-SF1	1.289	1.289	NRPMw	CE-20	3.375	$3.276^{+0.221}_{-0.09}$	89.078	10	$8.48^{+1.15}_{-1.78}$
14	DD2F-SF1	1.289	1.289	NRPMw_v1	ET	3.354	$3.243^{+0.066}_{-0.106}$	78.247	10	$8.40^{+1.23}_{-1.21}$
15	BLQ	1.298	1.298	NRPMw_v1	ET	2.927	$2.924^{+0.016}_{-0.025}$	93.474	10	$8.55^{+1.12}_{-1.65}$
16	BLh	1.298	1.298	NRPMw_v2	ET	2.804	$2.834^{+0.033}_{-0.025}$	89.049	10	$8.60^{+1.12}_{-1.62}$

1. Inspiral informed priors

Since the NR waveforms simulate only the last few orbits before merger and for a reliable estimate of masses and tidal parameters we require a longer inspiral data stream, we employ the TaylorF2 waveform model [115–121] to simulate the inspiral signal targeted at the parameters of the binaries listed in Table IV. The inspiraling binaries are assumed to be nonspinning and situated at the most optimal sky location corresponding to the detectors (either ET or CE).

We perform a self-consistent injection recovery with the TaylorF2 waveform model in the ET (or CE-40) noise configuration and compute posteriors on the chirp mass $\mathcal{M}_c$, tidal deformability $\tilde{\Lambda}$ as defined in Ref. [122], mass ratio q, individual tidal parameters Λ_is and the total mass M for all the hadronic models listed in Table IV. For this purpose, we employ the publicly available Bilby framework [123–125] that utilizes relative binning [126,127] for the computation of posteriors.

In Fig. 3, we show the posterior PDFs from the self-consistent injection recovery of the TaylorF2 model targeted to simulate a long inspiral of the $1.398M_\odot - 1.198M_\odot$ binary with the BLh EOS. We see that the chirp mass $\mathcal{M}_c$ is extremely well measured with a standard deviation of $6.77 \times 10^{-7} M_\odot$. The posterior PDFs for the tidal parameters Λ_is are refined by recomputing them via the universal relations presented in [128] by taking the M, q, Λ_1, and Λ_2 inspiral posteriors as inputs. This could be a potential source of systematic errors which we have underestimated given the uncertainties in these relations as pointed out in Ref. [129]. For comparison, we have presented the posteriors on Λ_is which have been obtained directly from the inspiral PE (not refined by the universal relations) and those which have been refined by the universal relations from [128] in Fig. 4. We note that this being an asymmetric merger ($q \neq 1$), we have an accurate determination of q and consequently Λ_1 and Λ_2. For an equal-mass merger, the injected value of $q = 1$, lies on the edge of the priors for the sampler, and the resulting posterior is one-sided as shown in Fig. 17. This one-sidedness of the mass ratio posterior also influences the measurement of Λ_1 and Λ_2 when refined by universal relations. Nevertheless, even for $q = 1$ mergers, symmetric tidal combinations such as κ_2^T, which is used as a probe for phase transitions, are estimated to be well within the 90% credible intervals.

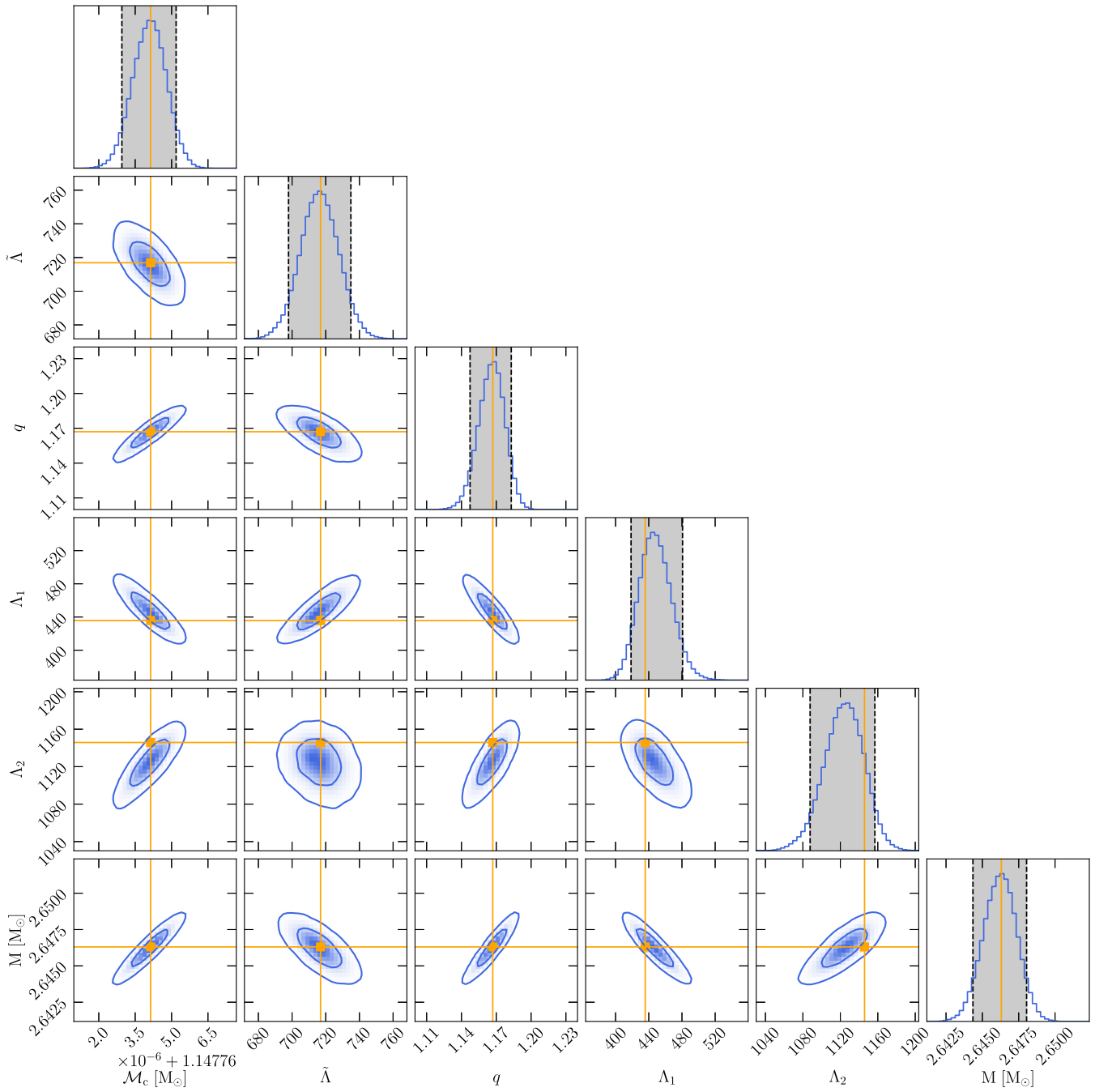

FIG. 3. Corner plot depicting the posteriors on chirp mass $\mathcal{M}_c$, tidal deformability $\tilde{\Lambda}$, mass ratio q, individual tidal parameters Λ_is and the total mass M for the binary $1.398M_\odot - 1.198M_\odot$ with the BLh EOS. These posterior PDFs are computed from a self-consistent injection recovery of the TaylorF2 waveform model corresponding to the binary parameters presented in Table I for the ET detector configuration. We show the 90% credible intervals in the 1D posteriors in gray shaded regions and the 50% and 90% credible contours for the 2D joint posteriors.

We approximate the inspiral posteriors on M, q, Λ_1, and Λ_2 with Gaussian distributions that have the same average as that of the inspiral posterior and a standard deviation equal to a quarter of the full 2σ width of the posterior. This choice allows us to be sufficiently conservative and establish a lower bound for measurement accuracy, which will only be improved if one chooses more restrictive priors and/or consider correlations between the priors. We remark that, at the moment, the BAJES infrastructure does not support a specification of correlated priors. We extract these Gaussian profiles from the simulations run with hadronic EOSs and use them as priors for a postmerger PE for both

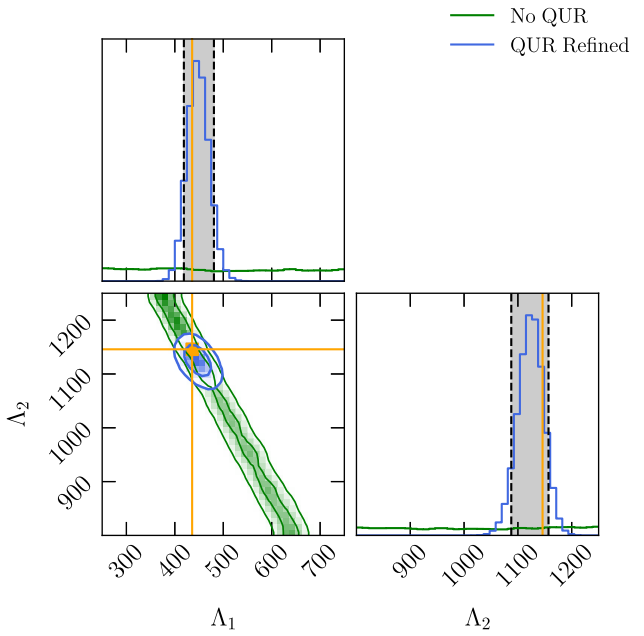

FIG. 4. A corner plot showing a comparison between measurements of tidal parameters Λ_1 and Λ_2 when computed directly from inspiral and when refined using quasiuniversal relations from [128].

hadronic and quark simulations. This is because, as discussed in Sec. II A, the hadronic and quark EOSs have the same low-density EOS and therefore the same tidal deformabilities. We would like to emphasize that while this approach is not a replacement for a full inspiral-postmerger inference, it provides reliable estimates for masses and tidal polarizabilities from the inspiral signal. The signal in the inspiral corresponding to a postmerger SNR of 10, has an SNR of ∼600. This corresponds to a detection rate of 0.5–1.5 yr^{-1} [12] with the ET detector and a detection rate of 1–1.5 yr^{-1} with the Cosmic Explorer CE-20 detector. The standard deviation in the inspiral estimates of the total mass ranges between $10^{-4}M_\odot - 10^{-3}M_\odot$. In addition to that, the percentage error in κ_2^T, i.e., deviation between the injected κ_2^T and the 50th percentile of the recovered posterior ranges from 0.1%–0.5%. The main advantage of employing a separate pipeline for the inspiral signal is the usage of relative binning which significantly reduces the computational cost. In addition, we have also shown an investigation of NRPMw's performance in tandem with the inspiral constraints.

2. Inspiral agnostic priors

We now describe the priors for the parameters of the NRPMw model in an inspiral-agnostic setting. These broad ranges on the priors have been taken from Ref. [71] to include a wide range of possibilities. Most importantly, the priors on M and q have been set according to [114] to maintain uniform priors on m_1 and m_2, the masses of the binary component stars. We also set uniform priors on Λ_is ranging from 0 to 4000 to cover a wide range in stellar compactness.

Providing a comparison between results obtained from an inspiral-informed and inspiral-agnostic choice of priors is essential. We present such a comparison of priors in Fig. 5. As we will make explicit in this work, the choice of priors has minimal influence on the recovery of f_2^{peak}, which is solely estimated from the postmerger. However, estimating f_2^{peak} is not the only prerequisite for detecting phase transitions. Phase transitions are detected by quantifying violations of EOS insensitive relations between the postmerger f_2 and the inspiral κ_2^T. With the inspiral-agnostic priors, f_2^{peak} is well measured but there are large uncertainties in the measurement of κ_2^T (see Appendix A). This can be mitigated by supplying priors that are informed about the tidal properties and masses from the inspiral signal. This is precisely what we observe with the choice of inspiral-informed priors where our sampler essentially recovers the Gaussian priors set from the inspiral on masses and tidal deformabilities. Another motivation behind such a comparative study with different choices of priors is to demonstrate the NRPMw model's performance when subjected to different degrees of independence in the sampling of the prior parameter space.

When a parameter of the NRPMw model is constrained by fits to EOS insensitive relations, we employ corresponding recalibration parameters to account for the uncertainties in these relations. The priors on all the recalibration parameters $\delta\boldsymbol{\theta}_{\mathrm{fit}}$ are distributed normally around a mean value of zero with a variance decided by the relative standard deviation between the scatter of NR simulations and the EOS insensitive relation. When we make a parameter independent of these fits as in the case of f_2, we ignore the corresponding recalibration parameter.

III. RESULTS

A. Inspiral-informed postmerger PE with Einstein Telescope

In this subsection, we present results for the postmerger PE analysis using the ET detector and by taking the priors on M, q, Λ_1, and Λ_2 as Gaussian (normal) distributions that are informed from the inspiral signal.

In Fig. 6, we show our results for an inspiral informed PE for the representative case of the $1.398M_\odot - 1.198M_\odot$ merger with the BLh and BLQ EOSs. We note that for the model with the BLQ EOS, the 90% credible interval (CI) estimated by NRPMw for the posterior of f_2^{peak} contains the injected value whereas for the model with the BLh EOS, the 95% CI of the f_2^{peak} posterior contains the injection. Additionally, in Fig. 7, we present the reconstructed frequency spectra for the same pair of simulations using NRPMw. We emphasize that the 90% CIs for f_2^{peak}

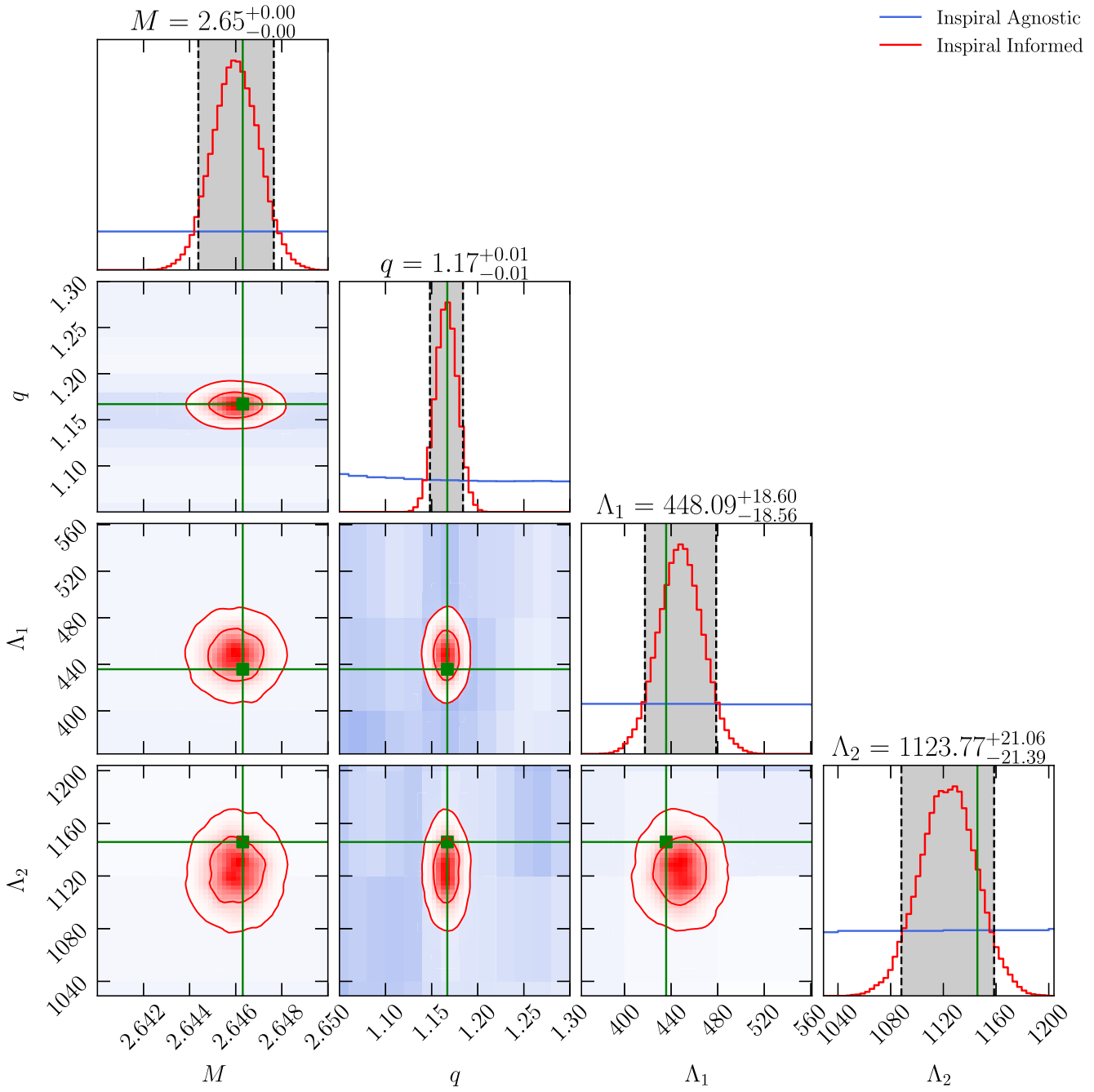

FIG. 5. A corner plot showing a comparison between the two types of priors employed in our work, i.e., a broad prior on M, q, Λ_1, and Λ_2 and Gaussian distributions informed of these quantities from an independent parameter estimation of the inspiral signal.

corresponding to the hadronic and quark cases do not overlap, implying that at a postmerger SNR of 10, the two models can be distinguished. In addition, we observe that the measurement of $f_2^{\rm peak}$ is insensitive (to within 90% CIs) to the choice of priors as it is an exclusively postmerger-determined quantity. The measurement of κ_2^T on the other hand improves substantially upon employing the inspiral informed priors as it is decided exclusively from the inspiral signal.

We summarize our results for the detectability of $f_2^{\rm peak}$ for all other simulations in our work in Figs. 18–20. We report that for the binaries $1.481M_\odot - 1.257M_\odot$ and $1.363M_\odot - 1.363M_\odot$ with the BLh EOS, the 90% CIs estimated for the $f_2^{\rm peak}$ posterior contain the injection. For the rest of the hadronic models, i.e., $1.398M_\odot - 1.198M_\odot$ with BLh, $1.289M_\odot - 1.289M_\odot$ with DD2F and $1.298M_\odot - 1.298M_\odot$ with BLh, 95%, 98%, and 99.5% CIs of $f_2^{\rm peak}$ contain the injection, respectively. For the

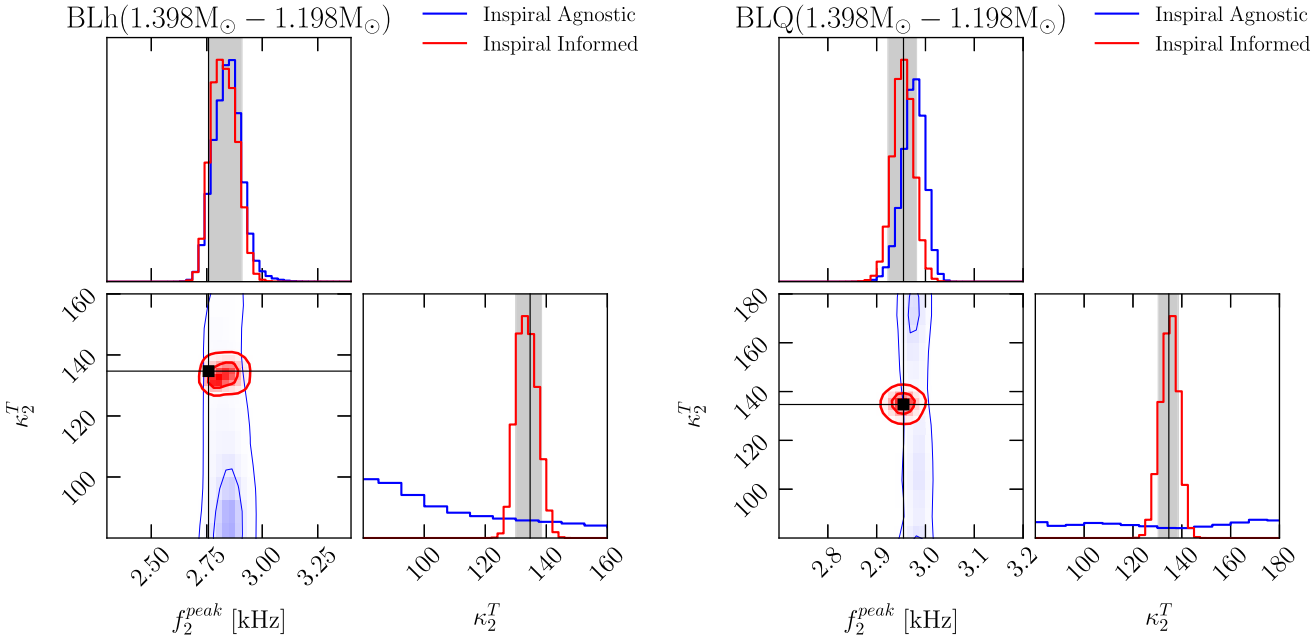

FIG. 6. Left panel: the posterior distribution on the postmerger peak frequency $f_2^{\rm peak}$ and the tidal polarizability κ_2^T for the binary $1.398M_\odot - 1.198M_\odot$ with the BLh EOS at a postmerger SNR of 10. We also show the 90% and 50% contour levels for the joint PDF. Additionally, we compare the posteriors obtained from the two choices of priors namely an inspiral agnostic choice (in blue) and an inspiral informed choice (in red). We observe that using inspiral informed priors has marginal influence on $f_2^{\rm peak}$ but substantially improves the measurement of κ_2^T as expected. Right panel: the same calculation for the corresponding quark model. Shown in gray shaded regions are the 90% CIs for the respective posteriors with inspiral informed priors. We note that for the quark EOS, NRPMw is able to recover the injected $f_2^{\rm peak}$ to within 90% CIs however, for the BLh (hadronic) case, the injected value lies at the boundary of the fifth percentile. Nevertheless, for both the cases the injection lies within the 90% contour of the joint PDF.

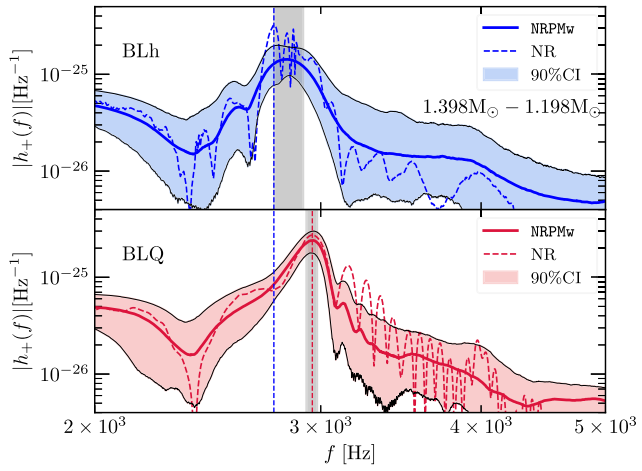

FIG. 7. Reconstructed spectra for the binary $1.398M_\odot - 1.198M_\odot$ with the BLh and BLQ EOSs at a postmerger SNR of 10. The dotted curves represent the injected spectra and the solid curves represent the median reconstructed signal by NRPMw. We also show 90% CIs on the reconstructed signal in the shaded regions. Vertical dotted lines correspond to the injected $f_2^{\rm peak}$ and the gray shaded regions represent the 90% CIs on the $f_2^{\rm peak}$ posteriors.

hadronic models, we identify a systematic bias that leads to an overestimation of $f_2^{\rm peak}$ by NRPMw. This bias primarily arises because of the presence of multiple (>2) amplitude modulations in the postmerger signal. As mentioned in Fig. 2 of Ref. [68], NRPMw is designed to capture the peaks of only the first two amplitude modulations, following which it models a damped sinusoidal decay of the postmerger amplitude. In the Sec. III A 1, we discuss this bias in detail. On the other hand, for the quark EOSs, we observe that the 90% CIs for $f_2^{\rm peak}$ contain the injected $f_2^{\rm peak}$ except for the $1.363M_\odot - 1.363M_\odot$ merger where the 95% CIs contain the injection.

1. Biases due to multiple amplitude modulations

A characteristic feature of our hadronic simulations, in particular the binaries $1.398M_\odot - 1.198M_\odot$ (BLh), $1.289M_\odot - 1.289M_\odot$ (DD2F), and $1.298M_\odot - 1.298M_\odot$ (BLh), is the existence of multiple amplitude modulations in the $\ell = 2$, $m = 2$ mode of the GW strain. From our NR simulations of hadronic EOSs, we note that these modulations are typically observed in the early postmerger signal, i.e., when the remnant has just formed and undergoes large dynamical deformations resulting in amplitude-modulated GW emissions. NRPMw, as of now, is unable to capture multiple modulations in the postmerger amplitude

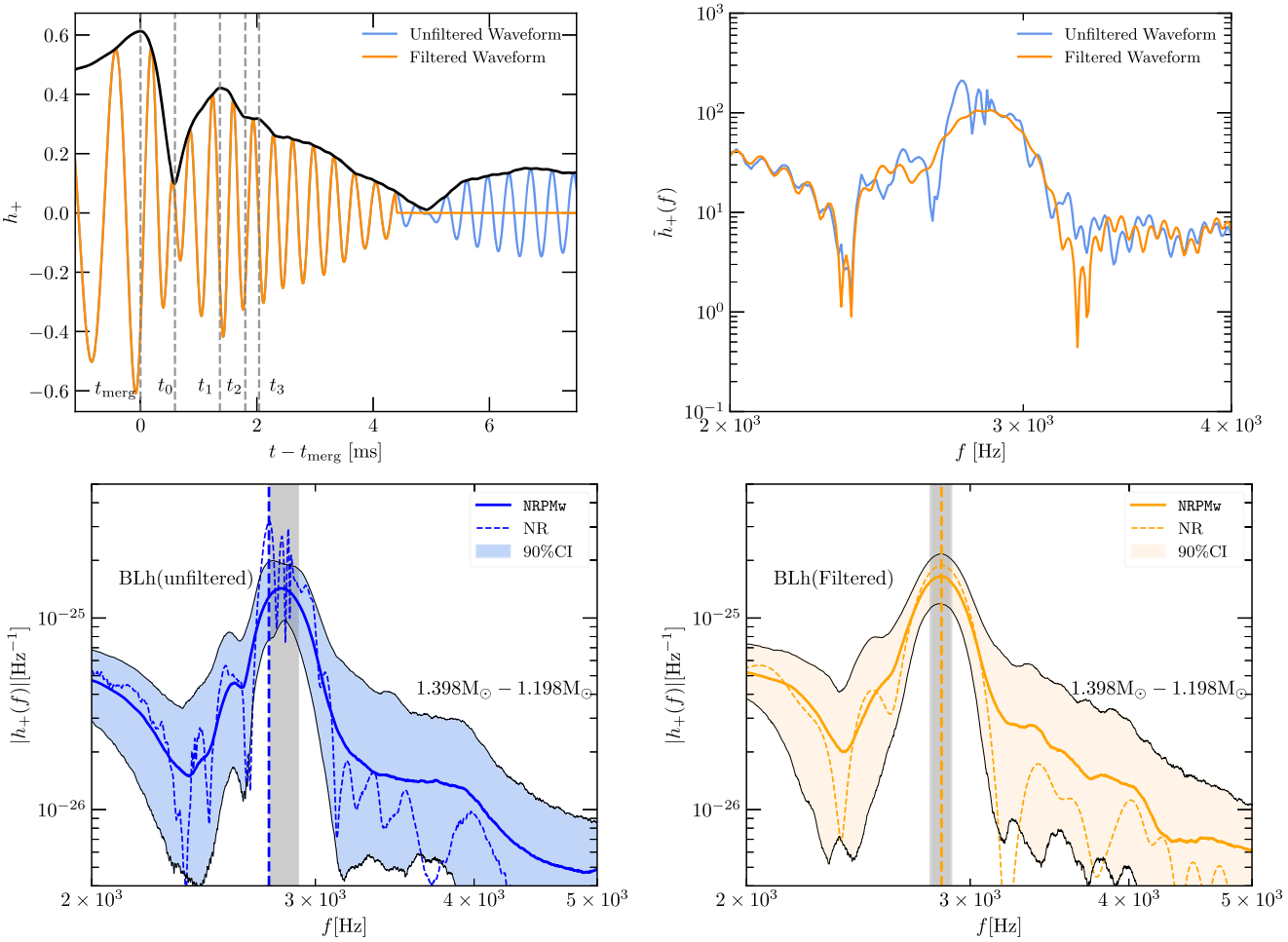

FIG. 8. Upper left panel: the time domain postmerger waveform for the BLh $1.398M_\odot - 1.198M_\odot$ binary with and without an exponential filter. NRPMw works best for the early postmerger where it can capture the first two amplitude modulations that peak at t_1 and t_3, respectively. The model, as of now, cannot capture subsequent amplitude modulations. Upper right panel: the frequency spectra of the corresponding unfiltered and filtered waveforms that show a shift in $f_2^{\rm peak}$ upon exclusion of amplitude modulations at $t - t_{\rm merg} \gtrsim 5$ ms. Bottom panel: the reconstructed spectra for the unfiltered waveform (left) and the filtered waveform (right) that show the bias in $f_2^{\rm peak}$'s measurement because of the third and subsequent amplitude modulations. We see that upon filtering these modulations, the model is able to capture the $f_2^{\rm peak}$ to within 90% CIs.

and attempts to reconstruct amplitude modulations beyond 2 via damped sinusoids. This leads to a biased overestimation of $f_2^{\rm peak}$ as is evidenced in Figs. 6, 18, and 19.

In this section, we explore in detail the major source of this systematic bias, i.e., the multiple amplitude modulations. In Fig. 8, we show the time domain waveform for the $1.398M_\odot - 1.198M_\odot$ binary with the BLh EOS that exhibits multiple amplitude modulations. In line with the convention for nodal points presented in Ref. [68], we denote positions of the merger as $t_{\rm merg}$, the first two postmerger maxima as t_1 and t_3 and their corresponding intermediate minima as t_0 and t_2. NRPMw only includes amplitude modulations until t_3 beyond which the amplitude is described by a damped sinusoid. We introduce an exponential filtering function

$$F(t) = 1/(1 + \exp(t - t_{\rm cutoff})), \tag{7}$$

where $t_{\rm cutoff}$ denotes the point where the filter cuts off the strain. We take $t_{\rm cutoff}$ to be near the position of the third amplitude modulation and filter off the subsequent signal to disentangle the effects of subsequent modulations. In the right panel of Fig. 8, we show the frequency spectra of this filtered waveform against that of the unfiltered waveform. We note that the subsequent amplitude modulations for $t - t_{\rm merg} \gtrsim 5$ ms lead to multiple oscillations near $f_2^{\rm peak}$. Such closely spaced oscillations in the frequency domain are not a morphology that can be captured by NRPMw and the model tends to construct an average over these peaks leading to a bias. On the other hand, when such

modulations have been filtered out, the model captures the peak of the filtered spectra much better.

We also refer the reader to Appendix C for a brief discussion on how one can start to mitigate this bias by modifying the NRPMw model and making it more flexible to capture multiple modulations.

We would like to emphasize that even though we have shown for our hadronic systems that removing multiple (>2) amplitude oscillations can help remove biases in the measurement of $f_2^{\rm peak}$, we only report results from the unfiltered, i.e., complete waveforms for the purposes of detecting phase transitions. This is because, in a realistic detection scenario, it is rather artificial to engineer the waveforms to support a recovery of $f_2^{\rm peak}$ to within some confidence level. Additionally, we would like to emphasize that there is still scope for improvement in the contemporary BNS waveform models to capture the above-mentioned morphologies and that additional avenues apart from shifts in $f_2^{\rm peak}$ need to be explored for a holistic examination of QCD phase transition effects.

B. Inspiral informed postmereger PE with Cosmic Explorer

In this subsection, we repeat the inspiral informed PE analysis described in Sec. III A on the $1.289M_\odot - 1.289M_\odot$ binaries with the DD2F and DD2F-SF1 EOSs but with a difference that now we employ the Cosmic Explorer sensitivities for recovering our models. The configurations we employ are a broad-band 40 km detector and a narrow-band 20 km detector which has been optimized for postmerger and has increased sensitivity in the 2–4 kHz regime. The advantage of the enhanced sensitivities of the CE-20 detector is that for the same postmerger SNR of 10, we will observe more distant and therefore more frequent mergers. We inject the TaylorF2 predicted inspiral for the hadronic model $1.289M_\odot - 1.289M_\odot$ with the DD2F EOS in the broad-band CE-40 configuration. This binary is now placed at a distance of 118.467 Mpc so as to produce a postmerger SNR of 10 in CE-20 configuration. This is because we would like to harness the sensitivities of the CE detectors most optimally. CE-40 has higher sensitivity at low frequencies corresponding to the inspiral signal and therefore it is utilized for estimating the mass and tidal parameters from an inspiral signal (as described in Sec. III A). On the other hand, CE-20 has increased sensitivities in the kilohertz regime corresponding to the emission frequencies of the BNS remnant and hence is utilized for the postmerger PE. For this analysis, we have assumed that both the CE-20 and CE-40 observatories are operating simultaneously and are located at the same position on Earth.

In Fig. 9, we present a reconstruction of the postmerger amplitude spectrum recovered using the CE-20 detector by the NRPMw model. We see yet again that the measurement

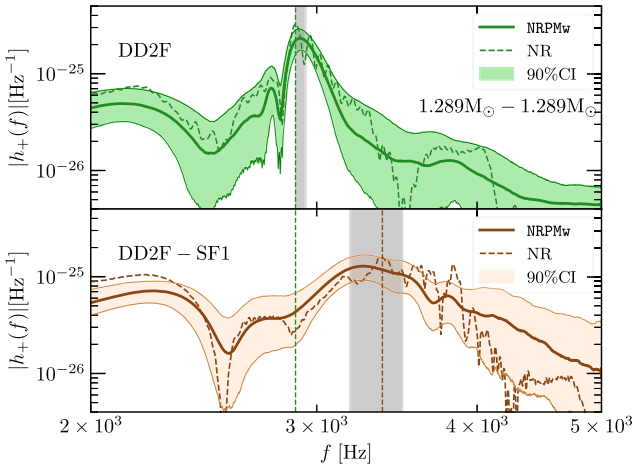

FIG. 9. The reconstructed spectra corresponding to an inspiral informed postmerger PE for the binary $1.289M_\odot - 1.289M_\odot$ with the DD2F and DD2F-SF1 EOSs, computed with the postmerger optimized CE-20 detector. Like in the case of recovery from Einstein Telescope (Fig. 20), here also we see that multiple amplitude modulations can bias the recovery of $f_2^{\rm peak}$ for DD2F.

of $f_2^{\rm peak}$ for the hadronic model is overestimated due to the multiple amplitude modulations in the time-domain GWs from the hadronic model which we show explicitly in Fig. 10. The quality of the reconstruction of spectra and the accuracy of recovery of $f_2^{\rm peak}$ is similar in both the ET and CE-20 detectors with the only advantage being the increased rates of observation of BNS mergers with CE-20.

So far we have demonstrated that the NRPMw model along with the sensitivities of the ET detector and the CE detector can reliably detect and reconstruct the postmerger signal which is evidenced by the fact that we recover most (≈8) of the injected SNR (Table IV). In addition, we have shown that our model is capable of recovering (albeit with some bias) the $f_2^{\rm peak}$ frequency and distinguishing the same between the hadronic and quark models at a postmerger SNR of 10. We would like to emphasize that detecting and distinguishing the $f_2^{\rm peak}$ frequency is not sufficient for inferring the occurrence of a phase transition in a realistic observational setting. The latter requires quantifying violations from EOS insensitive relations (see Sec. III C). Since such relations involve inspiral tidal parameters in addition to the postmerger $f_2^{\rm peak}$, it is imperative that we have reliable estimates of the tidal parameters. In this regard, the utility of inspiral informed priors becomes clear. We can see that for all our models be it hadronic or quark, the 90% CIs for κ_2^T posterior by the NRPMw model contain the injected value. There exists no information about masses or the tidal properties from the postmerger signal alone (at least at a postmerger SNR of 10) and our postmerger model essentially recovers these priors. In contrast, with the priors that are agnostic of the inspiral

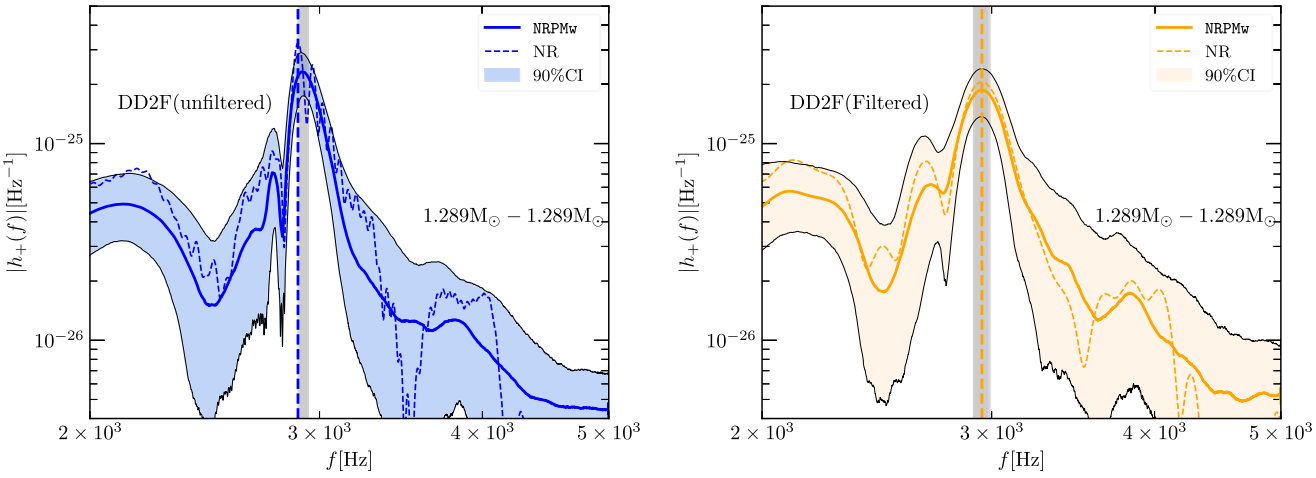

FIG. 10. Same calculation as in Fig. 8 to show the impact of multiple amplitude modulations on the recovery of $f_2^{\rm peak}$ for the hadronic DD2F simulation computed with the CE-20 detector. Here also we observe that filtering out the third and subsequent modulation in the postmerger amplitude can result in an accurate recovery of $f_2^{\rm peak}$ to within 90% CIs.

signal, as in Appendix A, the estimates of the tidal κ_2^T are dominated by large errors which in turn will make an inference of QCD phase transitions difficult from the EOS insensitive quasiuniversal relations.

C. Probing QCD phase transitions

As we have previously remarked, detection of a postmerger signal and a reliable recovery and distinguishability of $f_2^{\rm peak}$ is necessary but not sufficient for probing QCD phase transitions. Previous works [41,42,72] suggest the utility of EOS insensitive relations, in particular between $f_2^{\rm peak}$ and a tidal parameter be it $\tilde{\Lambda}$ or κ_2^T, in probing such phase transitions. Specifically, if EOS softening effects by such phase transitions produce deviations from the aforementioned relations that are nondegenerate with other hadronic models, one can ascertain the occurrence of a phase transition with some confidence. This requires that we have reliable estimates of not just $f_2^{\rm peak}$ but also of tidal properties. Comparing NR simulations of the postmerger signal at different resolutions can only provide the former as a one-dimensional error estimate because tidal properties are fixed upon assuming a specific equation of state. The only way we can compute a joint uncertainty of $f_2^{\rm peak}$ and κ_2^T is by Bayesian inference of the postmerger signal that is informed of the tidal properties from the inspiral (and of course a Bayesian inference on the full signal).

We employ the fitting function obtained in Ref. [68] with reference to the CoRe database. This fitting function improves upon the QUR obtained in Ref. [67] by explicitly including the effects of inspiral spins and taking into account additional GRHD simulations performed with WhiskyTHC and BAM infrastructures. In Fig. 11, we plot the QUR fitting function for symmetric binaries that are nonspinning, along with an ensemble of simulations that form a part of the CoRe database. We also show the 90% confidence levels for the fit describing symmetric binaries. To this collection, we add the injections presented in this work with their error estimates that are essentially the 90% contour levels of the two-dimensional joint posteriors for mass-rescaled $Mf_2^{\rm peak}$ and κ_2^T obtained with the choice of inspiral informed priors.

In Sec. III A and Appendix B, we have provided evidence for mutual distinguishability between hadronic and quark models based on the nondegeneracy of the 90% CIs of the $f_2^{\rm peak}$ posteriors. In this section, we present a discussion on detecting phase transitions based on nondegeneracies between the joint $f_2^{\rm peak} - \kappa_2^T$ posteriors and comparing them with the EOS insensitive relation of Breschi *et al.* [68]. In the first (upper-left) panel of Fig. 11, we present hadronic and quark models that, at a postmerger SNR of 10, are mutually distinguishable as is seen by the absence of any overlap between the corresponding joint $Mf_2^{\rm peak} - \kappa_2^T$ posteriors. These models are the $1.363M_\odot - 1.363M_\odot$ binary for the BLh and BLQ EOSs and the $1.289M_\odot - 1.289M_\odot$ binary for the DD2F and DD2F-SF1 EOSs. For the $1.363M_\odot - 1.363M_\odot$ binary, we notice that even though the hadronic and quark models are distinguishable (up to 90% confidence), the quark model's joint posterior is degenerate with other hadronic EOSs, implying that a postmerger SNR of 10, we cannot conclusively confirm a phase transition for this binary. On the other hand, for the $1.289M_\odot - 1.289M_\odot$ binary with the DD2F-SF1 EOSs, we notice that the injection and the corresponding joint posteriors do not overlap with the universal relation, implying that at a postmerger SNR of 10, we can confirm the presence of a phase transition. We do however caution the reader about a possible caveat. The conclusion that whether we can confirm a phase transition to some confidence is sensitive

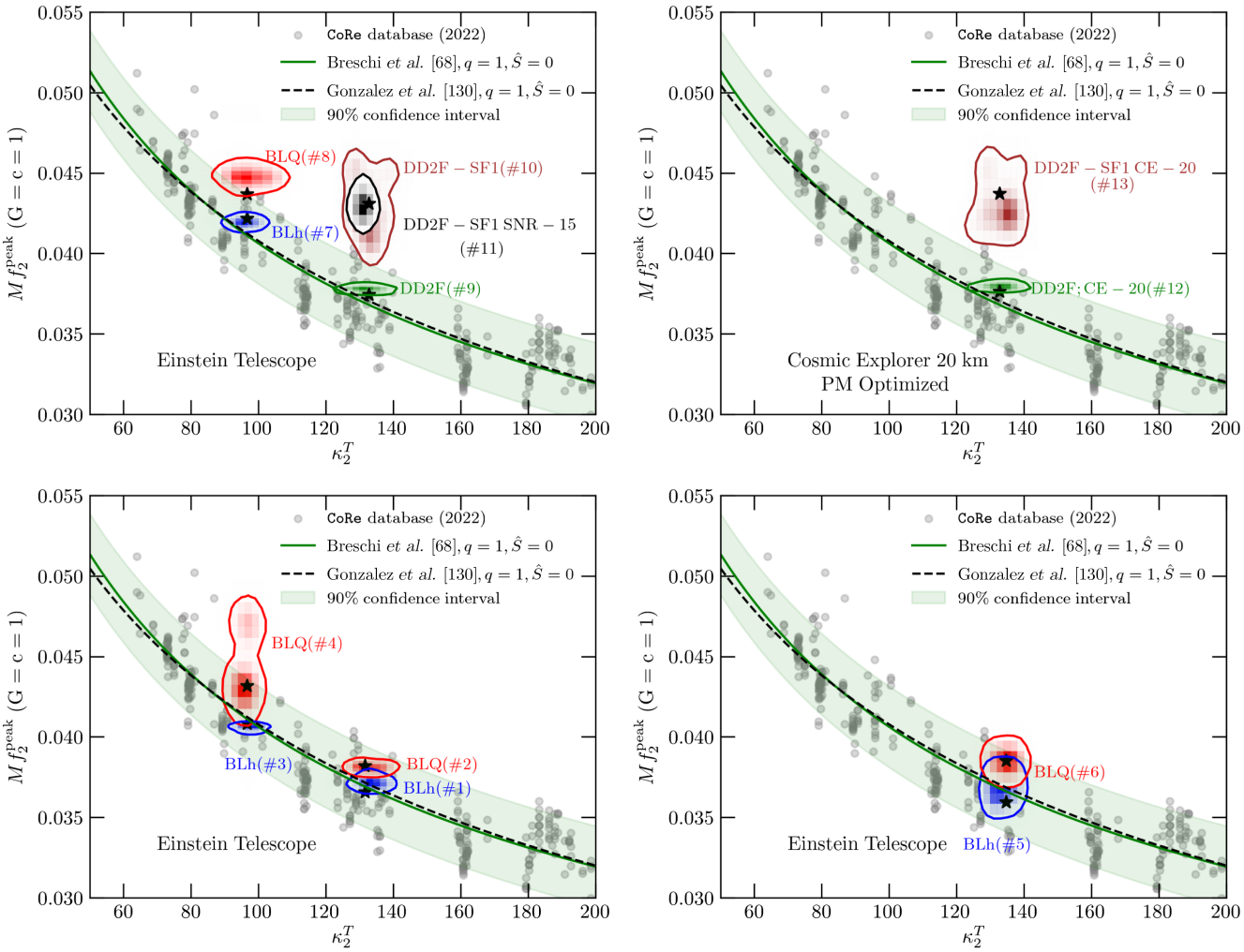

FIG. 11. Quasiuniversal relation from Breschi *et al.* [68] shown along with this work's Bayesian inference error estimates. Shown in gray scatter points, are the hadronic simulations from the CoRe database along with the fitting functions from [68,130] for nonspinning and symmetric binaries. The light green shaded region represents a 90% confidence interval corresponding to the fit function from [68] which is also implemented in the NRPMw model. Even though [130] updates upon the fit coefficients in [68], the two are within 90% confidence of each other. Black stars denote the injected values in a 2D parameter space of Mf_2 and κ_2^T. The colored shaded regions represent the 90% contours of the 2D joint posteriors on Mf_2 and κ_2^T obtained in this study. In parenthesis we depict the simulation index of the binaries as defined in Table IV. Top panels: we show binaries which are nondegenerate with respect to each other up to 90% CIs and with the universal relation. Bottom panels: we show models which are not mutually distinguishable to 90%.

to the particular universal relation used. The 90% contours of the joint posterior with DD2F-SF1 EOS, even though not overlapping with the universal relation's error margin, are very close to them and systematics in the universal relation may change our conclusions. Such systematics may result from updating the coefficients of the fit upon adding more simulations. At higher postmerger SNRs, detectability avenues will improve. This is made concrete by an additional model recovered at a higher postmerger SNR of 15, where we find that the DD2F-SF1 model's joint posteriors shrink and are even more removed from the universal relation than the same model at postmerger SNR 10.

Similarly, in the second panel (top right) of the Fig. 11, we repeat the calculations for the case of $1.289M_\odot - 1.289M_\odot$ binary with the DD2F and DD2F-SF1 EOS, assuming the Cosmic Explorer (CE-20) detector sensitivity. We notice here that the joint posteriors corresponding to the quark EOS are "more" nondegenerate with the universal relation as compared to the same model recovered from the Einstein Telescope sensitivity. Consequently, at a postmerger SNR of 10, we can confirm the presence of a phase transition. The better performance of the CE-20 detector as compared to the Einstein Telescope's recovery, is not entirely unexpected. Indeed we note that for the injected $f_2^{\rm peak}$ frequencies close to 3 kHz, the CE-20 detector is more sensitive than the ET detector.

On the other hand, in the third (bottom left) and fourth (bottom right) panels of Fig. 11, we show binaries for

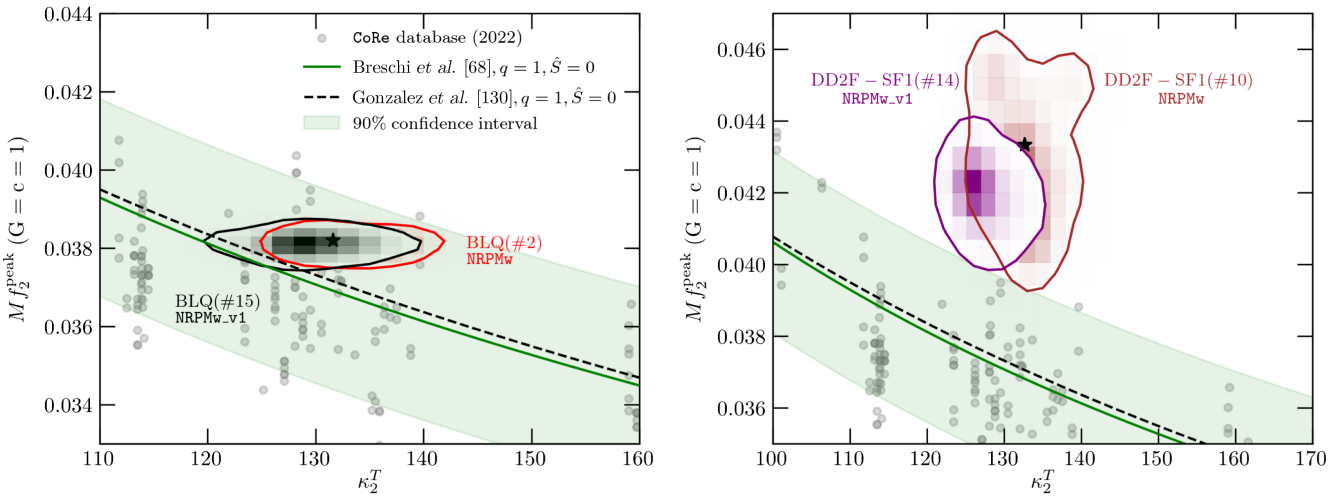

FIG. 12. A comparison of the joint inference of $f_2^{\rm peak}$ and κ_2^T between two configurations of NRPMw, i.e., excluding the $f_2^{\rm peak} - \kappa_2^T$ universal relation (NRPMw) and including the $f_2^{\rm peak}$ universal relation (NRPMw_v1). Left panel: results for the $1.298M_\odot - 1.298M_\odot$ binary with the BLQ EOS whose injection follows the universal relation. Both the model configurations can recover the injection with the data (injection) slightly preferring the QUR informed model NRPMw_v1. Right panel: results for the $1.289M_\odot - 1.289M_\odot$ binary with the DD2F-SF1 EOS whose injection strongly violates the universal relation. The data (injection) slightly prefers the more flexible QUR uninformed model (NRPMw) as it has larger flexibility than NRPMw_v1 in reference to recovering injections that violate the universal relation.

which the 90% contours of the joint posterior overlap between the hadronic and quark models. These models include the $1.298M_\odot - 1.298M_\odot$, $1.481M_\odot - 1.257M_\odot$, and $1.398M_\odot - 1.198M_\odot$ binaries with the BLh and BLQ EOSs. For the quark models of these binaries, at a postmerger SNR of 10, the presence of a QCD phase transition cannot be ascertained given the degeneracy with other hadronic EOSs.

Therefore, in a nutshell, even though postmerger waveforms from the hadronic models may be distinguishable from the corresponding quark models by virtue of nondegeneracy of $f_2^{\rm peak}$ posteriors, they may still be degenerate with each other in a two-dimensional space of $f_2^{\rm peak} - \kappa_2^T$ uncertainties. Furthermore, when there is no degeneracy in a joint measurement of $f_2^{\rm peak}$ and κ_2^T, a postmerger SNR of 10 can confirm the presence of a phase transition only if the model violates the universal relation strongly, i.e., $\Delta f_2^{\rm peak} \approx 455$ Hz ($\gtrsim 1.6\sigma$). At a postmerger SNR of 10, systematics in the universal relation may also play a role in influencing conclusions about the detectability of phase transitions. However, for louder binaries with SNR ~ 15, phase transitions of the type predicted by the DD2F-SF1 model can be confirmed with a higher confidence.

At this stage we also present a test of the EOS insensitive relations with reference to detecting QCD phase transitions in Fig. 12. To this aim, we test two configurations of our model. First, we use the NRPMw configuration employed throughout this work where the f_2 parameter is independent of the $f_2 - \kappa_2^T$ universal relation from Breschi *et al.* [68], i.e., the universal relation is ignored. Secondly, we employ the original model configuration of Breschi *et al.* (called NRPMw_v1 in this work) where f_2 is decided by the universal relation. In particular, we are posing the question that given a signal, whether the inclusion of the $f_2 - \kappa_2^T$ universal relation in the model can play a role in detecting a "strong" phase transition. In the left panel of Fig. 12, we present results for the $1.298M_\odot - 1.298M_\odot$ binary with the BLQ EOS whose injection is consistent with the universal relation. We note that for both model configurations, the 90% contour of the joint PDF contains the injection at a postmerger SNR of 10. To quantify this comparison we compute the Bayes' factor for the two hypotheses, i.e., inference with and without the universal relation, respectively. We find that $\log \mathcal{B}^{\rm with\,QUR}_{\rm without\,QUR} = 2.53^{+0.27}_{-0.27}$ indicating a weak preference towards the QUR informed NRPMw_v1 model. On the other hand, in the right panel of Fig. 12, we present the same calculation for the $1.289M_\odot - 1.289M_\odot$ binary with the DD2F-SF1 EOS. Since in this case, the injection is inconsistent with the universal relation, including the same in the model tends to drive the joint posterior toward the universal relation and away from the injection. This is evidenced by the fact that the 90% contour of the NRPMw_v1 model does not contain the injection whereas the injection is well captured within the joint posterior of the more flexible NRPMw model. To quantify the same statement, the $\log \mathcal{B}^{\rm without\,QUR}_{\rm with\,QUR} = 2.24^{+0.27}_{-0.27}$ at a postmerger SNR of 10 indicating a weak preference towards the more flexible NRPMw model with respect to detecting phase transitions that strongly violate the universal relations.

IV. CONCLUSIONS

In this work, we have shown that the next generation of GW experiments has the potential to identify QCD phase transitions in the postmerger phase of neutron star mergers, provided such phase transitions are sufficiently strong.

To model the influence of deconfined quarks on the dynamics of BNS merger remnants, we employ the BLQ and DD2F-SF1 EOSs which model the deconfined quark phase by Gibbs construction and Maxwell's construction respectively. In the case of a merger, these treatments lead to remnants with very different properties, most notably differences in the postmerger peak frequencies. We construct the postmerger signals by windowing out the inspiral signal from our NR waveforms and injecting the signal thus obtained in a noise-less configuration of ET or CE detectors.

We perform independent Bayesian inference calculations on the inspiral and the postmerger signals using the Bilby (via the TaylorF2 model) and BAJES (via the NRPMw model) codes, respectively. We compute the posteriors of total mass, mass ratio and tidal deformabilities which are expectedly Gaussian to a good approximation (except for the one-sided $q = 1$ posteriors). These posteriors help inform the priors for the postmerger PE analysis which provides the posteriors on $f_2^{\rm peak}$. We find that NRPMw model can reliably recover the postmerger signal as is evidenced by the recovered SNRs (Tables IV and V). Additionally, at a postmerger SNR of 10, the model can also recover the $f_2^{\rm peak}$ frequency and distinguish the same between a hadronic and quark model to up to 90% confidence.

Our work also serves to present new test cases to which our waveform model has been applied as a means to evaluate its validity. We have presented for the first time, the behavior of the model in an inspiral-informed PE setting and tested its performance on morphologically complex NR waveforms. It is noteworthy that simulations from DD2F, DD2F-SF1 EOSs are also the ones that the model has not been trained on. For these cases too we get reliable signal reconstruction and recover most of the SNR.

We have provided a complimentary analysis by employing the CE-40 and CE-20 detectors. The advantage of utilizing the CE detectors for this purpose is twofold. First, with enhanced postmerger sensitivities, BNS mergers can be probed at larger luminosity distances and hence more frequently. Second, a combination of broad-band CE-40 detector and a narrow-band postmerger optimized CE-20 detector is optimal for a holistic detection because of increased sensitivities in the inspiral (by CE-40) and the postmerger (by CE-20). For sources with postmerger SNR of 10 in CE-20, we have used the CE-40 detector to compute posteriors on masses and tidal parameters that serve as priors on the postmerger PE analysis via the CE-20 detector. We find no major differences in the inference of $f_2^{\rm peak}$ or the quality of signal reconstruction as compared to inference with the ET detector.

We emphasize that even though NRPMw coupled with the enhanced sensitivities of the upcoming generation of GW detectors, can reliably detect and distinguish the $f_2^{\rm peak}$ frequencies at a postmerger SNR of 10, it is not sufficient to probe QCD phase transitions. We compare the joint posterior estimates on $f_2^{\rm peak}$ and κ_2^T in reference to the $f_2 - \kappa_2^T$ universal relation from Breschi *et al.* [68] and find that starting at postmerger SNRs of 10, we can claim a detection of a first order phase transition but only for models that violate the universal relations by more than 1.6σ. We also demonstrate a slight preference towards the model configuration which is independent of the universal relation in detecting "strong" phase transitions by a $\log \mathcal{B}^{\rm without\,QUR}_{\rm with\,QUR} = 2.24^{+0.27}_{-0.27}$.

For final remarks, Bayesian inference is done on waveforms that have a rich morphological structure and therefore we speculate that indicators of QCD phase transitions may not be exclusively encoded in $f_2^{\rm peak}$. This warrants exploration of alternative signatures of phase transitions, e.g., imprints in the postmerger amplitude or the lifetimes of remnants. Our work calls for efforts in several directions. First, as we have shown, the current waveform models need to be improved to take into account additional waveform morphologies like multiple amplitude modulations which can be a significant source of bias at high enough SNRs. Additionally, a prescription for modeling the high-frequency black hole ringdown spectrum can be accommodated in NRPMw; however, we have omitted the same in favor of ease of computation. The ringdown spectrum and the ensuing quasinormal modes can be important for constraining QCD phase transitions from short-lived remnants or promptly collapsing binaries where such phase transitions can play a role [105,106,131]. Second, the universal relations can themselves involve systematic biases that can be sourced from uncertainties in the physics modeled in the simulations. Such biases may shift the universal relations in the $f_2^{\rm peak} - \kappa_2^T$ plane affecting conclusions about the occurrence of phase transitions. On a related note, it is also anticipated that modified-gravity theories [132] can distort the interpretation of tidal parameters [133] and produce effects [134] that may mimic QCD phase transitions.[1] Lastly, improvements are required in improving the postmerger convergence of contemporary NR codes [136] as will be required by large SNR detections from the next generation detectors. Overall, the prospects of detecting a QCD phase transition with the enhanced sensitivities of the upcoming detectors, seem not too pessimistic. A single GW170817-like event, provided a postmerger is also observed, can in theory constrain QCD phase transitions.

[1]See also [135].

ACKNOWLEDGMENTS

A. P. would like to thank Alejandra Gonzalez for providing the postmerger data from the second release of the CoRe database for the updated fits in Fig. 11. A. P. would also like to thank Professor K. G. Arun and Dr. Arnab Dhani for many useful discussions, a careful reading of the manuscript and their comments. D. R. acknowledges funding from the U.S. Department of Energy, Office of Science, Division of Nuclear Physics under Award No. DE-SC0021177 and from the National Science Foundation under Grants No. PHY-2011725, No. PHY-2020275, No. PHY-2116686, and No. AST-2108467. D. R. acknowledges support as an Alfred P. Sloan Fellow. Simulations were performed on PSC Bridges2, SDSC Expanse, TACC's Stampede2 (NSF XSEDE allocation TG-PHY160025). This research used resources of the National Energy Research Scientific Computing Center, a DOE Office of Science User Facility supported by the Office of Science of the U.S. Department of Energy under Contract No. DE-AC02-05CH11231. Computations for this research were performed on the Pennsylvania State University's Institute for Computational and Data Sciences' Roar supercomputer. S. B. acknowledges funding from the EU Horizon under ERC Consolidator Grant No. InspiReM-101043372.

APPENDIX A: INSPIRAL AGNOSTIC PE: RESULTS FOR ALL SIMULATIONS

In this appendix, we present results for a postmerger PE of the NRPMw model's parameters wherein we set a wide range of values to the priors as described in Table II. The choice of priors follows that in [71] and is targeted at a wide range of possibilities for the GW event. To this aim, we present results for the postmerger PE of all the simulations listed in Table V performed with this choice of priors. In Figs. 13–15 we present the posterior PDFs for $f_2^{\rm peak}$ and κ_2^T. We note that the $f_2^{\rm peak}$ frequencies are recovered accurately and the injection is contained in the 90% CIs. There appear to be no significant differences as compared to the estimation of $f_2^{\rm peak}$ from the inspiral informed choice of priors. At the same time, κ_2^T is very poorly determined, serving to verify the fact that once the $f_2 - \kappa_2^T$ universal relation has been omitted from the model, there exists no tidal information solely from the postmerger signal.

Finally, in Fig. 16, we present the waveform reconstruction for the case of inspiral agnostic priors. Like in the case of the inspiral informed priors, the postmerger estimation of $f_2^{\rm peak}$ is accurate and distinguishable between hadronic and quark models. Additionally, the signal is reliably reconstructed as shown by the fact that most of the postmerger SNR is recovered (see Table V).

APPENDIX B: INSPIRAL INFORMED PE: RESULTS FOR ALL SIMUATIONS

In this appendix, we present results analogous to Figs. 6 and 7 for all the systems as listed in Table IV with the ET detector and the NRPMw model at a postmerger SNR of 10. In particular, in Figs. 18 and 19 we show the posterior PDFs for $f_2^{\rm peak}$ and κ_2^T. As mentioned previously in Sec. III A, the NRPMw model performs very well with the quark EOSs, in that the 90% CI of $f_2^{\rm peak}$ posteriors contain the injection. However, for the hadronic simulations $1.398M_\odot - 1.198M_\odot$ (BLh), $1.289M_\odot - 1.289M_\odot$ (DD2F), and $1.298M_\odot - 1.298M_\odot$ (BLh), the estimation of $f_2^{\rm peak}$ is biased due to the presence of multiple amplitude modulations as explained in Fig. 21. We also show postmerger spectra for the waveform reconstructions in Fig. 20 that serve to reaffirm the detectability and distinguishability of the $f_2^{\rm peak}$ frequencies between the hadronic and quark models.

TABLE V. Same properties as presented in Table IV but now for the choice of inspiral agnostic priors.

Index	EOS	$m_1\,[M_\odot]$	$m_2\,[M_\odot]$	GW Model	Detector	$f^{\rm peak}_{2;\rm Injected}$ [kHz]	$f^{\rm peak}_{2;\rm Recovered}$ [kHz]	D_ℓ [Mpc]	$\rho_{\rm injected}$	$\rho_{\rm recovered}$
1	BLh	1.298	1.298	NRPMw	ET	2.804	$2.825^{+0.033}_{-0.025}$	89.049	10	$8.88^{+1.07}_{-1.59}$
2	BLQ	1.298	1.298	NRPMw	ET	2.927	$2.924^{+0.025}_{-0.025}$	93.474	10	$8.64^{+1.08}_{-1.61}$
3	BLh	1.481	1.257	NRPMw	ET	2.962	$2.957^{+0.016}_{-0.025}$	97.503	10	$8.79^{+1.12}_{-1.47}$
4	BLQ	1.481	1.257	NRPMw	ET	3.143	$3.284^{+0.139}_{-0.246}$	83.434	10	$8.72^{+1.15}_{-1.11}$
5	BLh	1.398	1.198	NRPMw	ET	2.758	$2.842^{+0.098}_{-0.09}$	87.027	10	$7.89^{+0.88}_{-1.15}$
6	BLQ	1.398	1.198	NRPMw	ET	2.955	$2.973^{+0.033}_{-0.033}$	87.500	10	$8.66^{+1.22}_{-1.43}$
7	BLh	1.363	1.363	NRPMw	ET	3.073	$3.055^{+0.025}_{-0.033}$	97.282	10	$7.97^{+1.19}_{-1.52}$
8	BLQ	1.363	1.363	NRPMw	ET	3.197	$3.284^{+0.279}_{-0.147}$	78.449	10	$8.13^{+1.21}_{-1.29}$
9	DD2F	1.289	1.289	NRPMw	ET	2.889	$2.907^{+0.025}_{-0.025}$	93.284	10	$8.51^{+1.12}_{-1.48}$
10	DD2F-SF1	1.289	1.289	NRPMw	ET	3.354	$3.432^{+0.066}_{-0.139}$	78.247	10	$8.60^{+1.38}_{-1.20}$

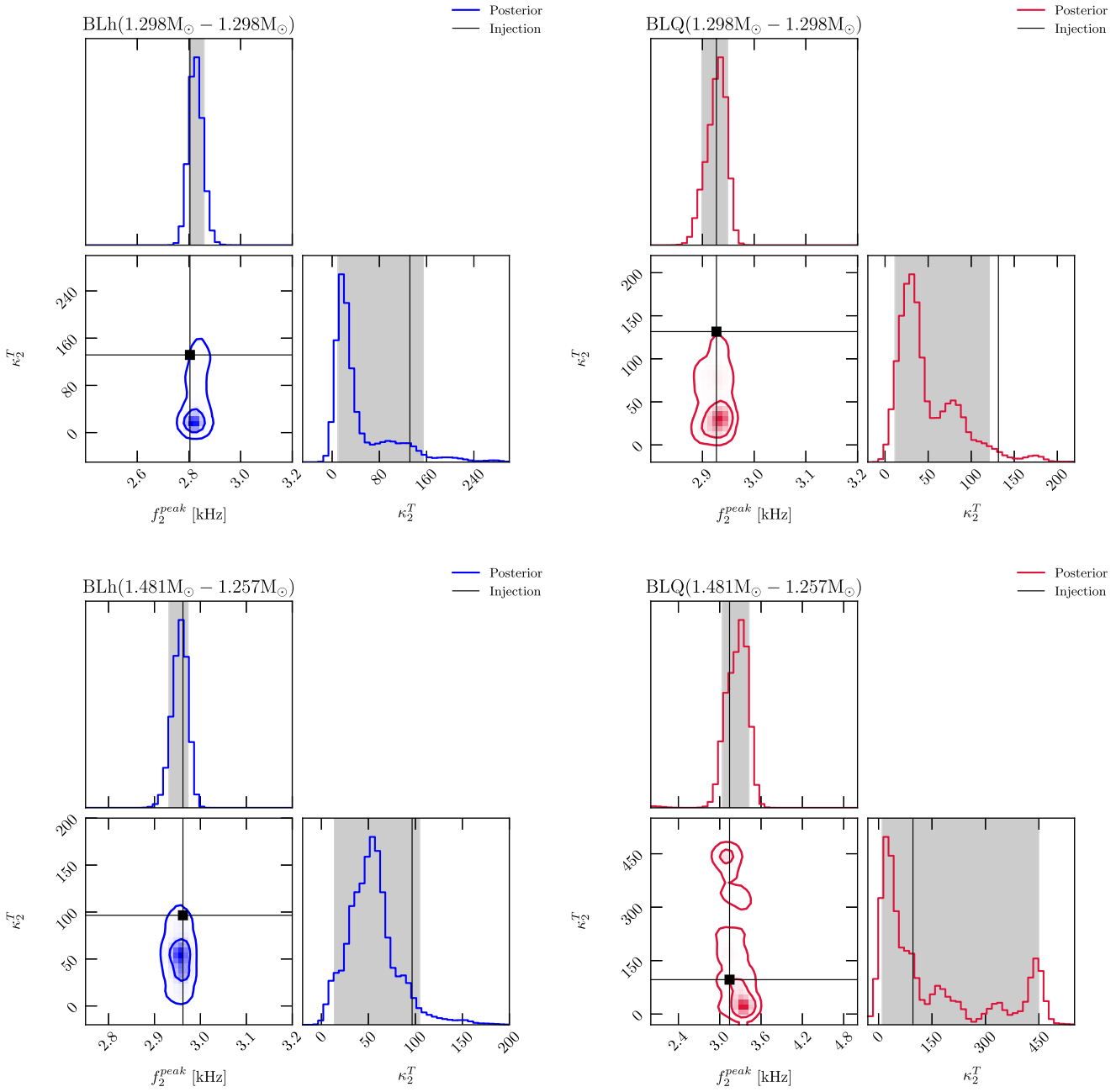

FIG. 13. Same calculations as in Fig. 6, i.e., a measurement of $f_2^{\rm peak}$ and κ_2^T for the $1.298M_\odot - 1.298M_\odot$ and $1.481M_\odot - 1.257M_\odot$ binaries with the BLh and BLQ EOSs. In contrast to Fig. 6, here we use a different choice of priors that are uninformed of the inspiral signal and set to wide ranges as described in Table II. We note that the NRPMw model captures to within 90% CIs the $f_2^{\rm peak}$ frequency for the quark and hadronic models; however, the tidal polarizability κ_2^T is poorly determined owing to the fact that no tidal information is present in the postmerger signal.

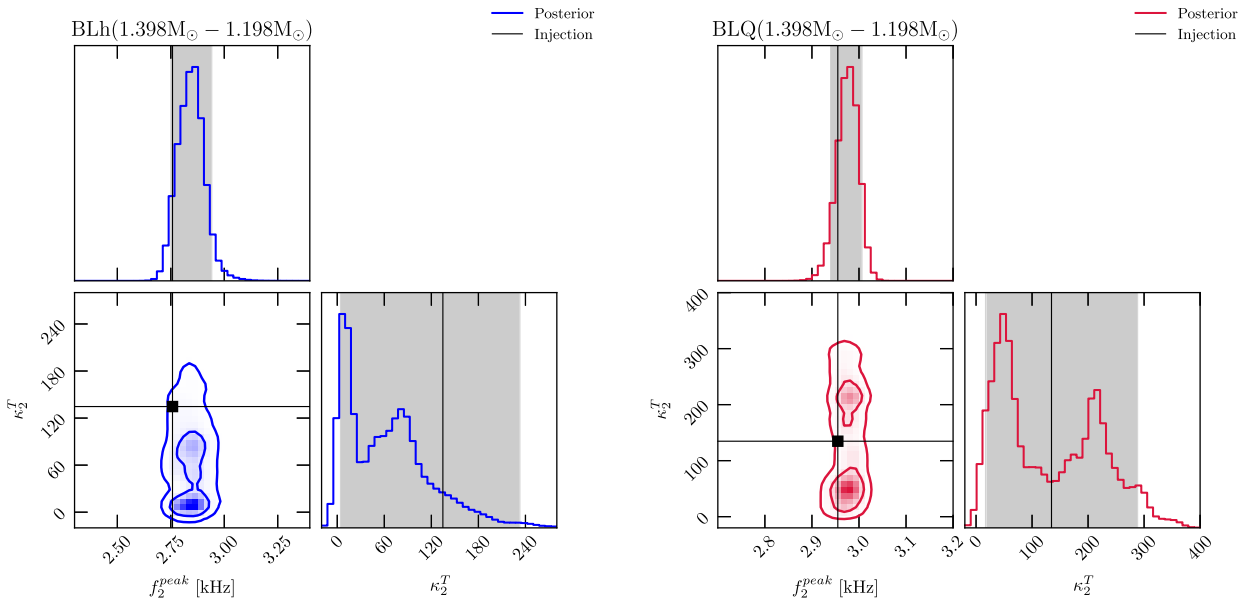

FIG. 14. Same calculations as in Fig. 13 for the binary $1.398M_\odot - 1.198M_\odot$ simulated with the BLh and BLQ EOSs.

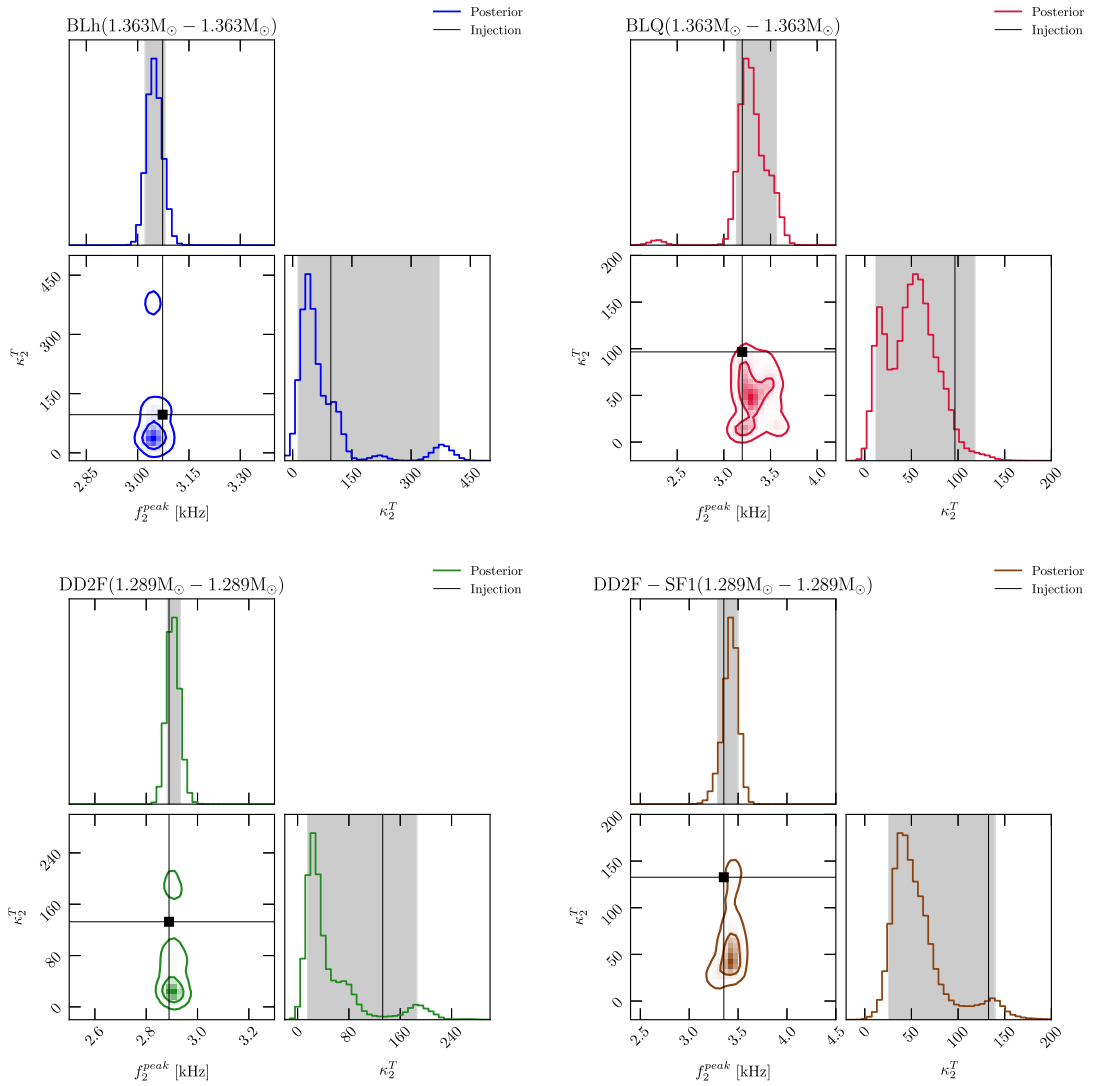

FIG. 15. Same calculations as in Fig. 13 for the binary $1.363M_\odot - 1.363M_\odot$ simulated with the BLh and BLQ EOSs and the binary $1.289M_\odot - 1.289M_\odot$ simulated with the DD2F and DD2F-SF1 EOS.

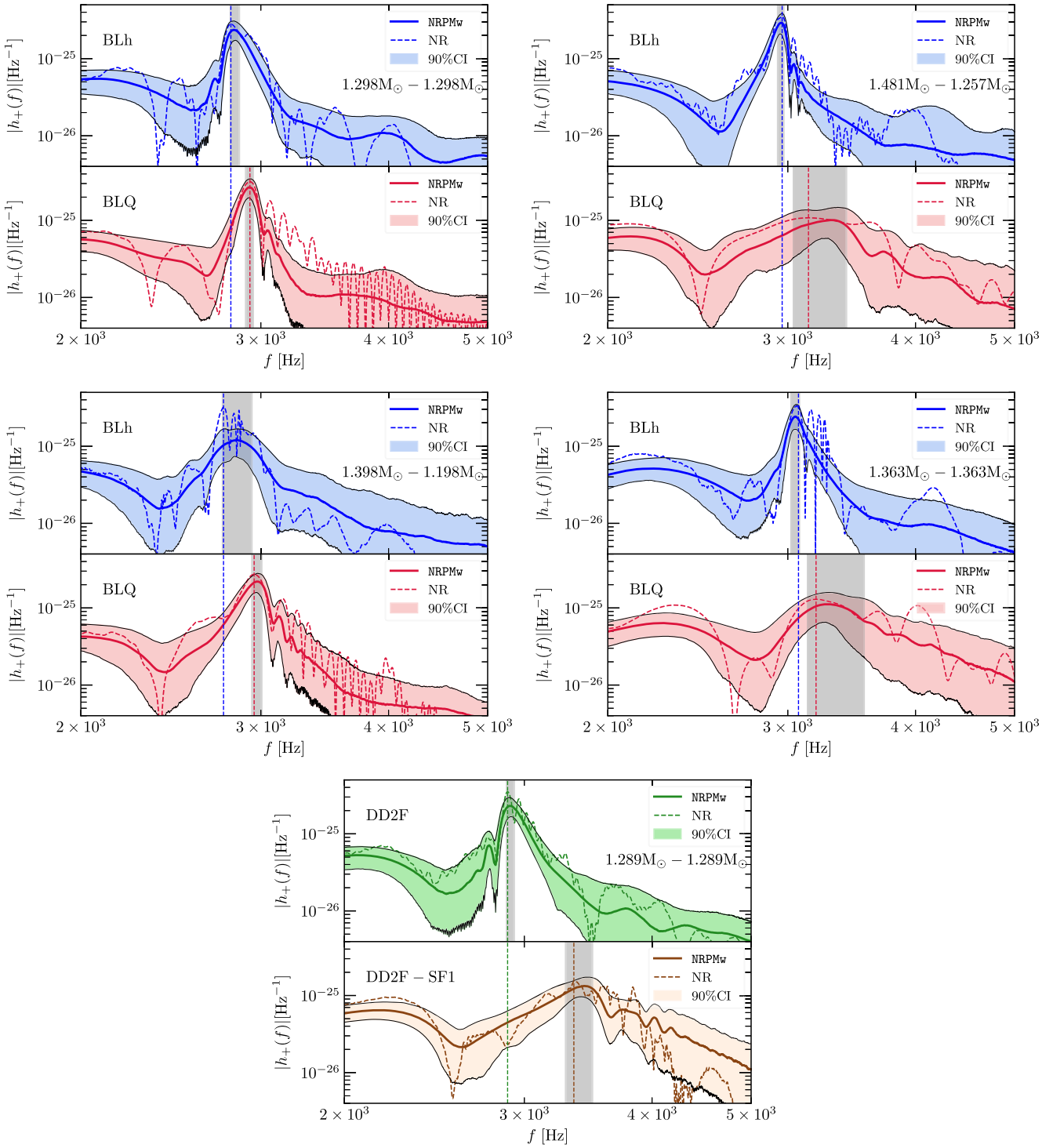

FIG. 16. Same calculation as in Fig. 7, i.e., reconstructed spectra for all the binaries in our work but computed with priors that are uninformed of the inspiral signal. We observe an accurate recovery of f_2^{peak} and distinguishability between hadronic and quark models to 90% at a postmerger SNR of 10.

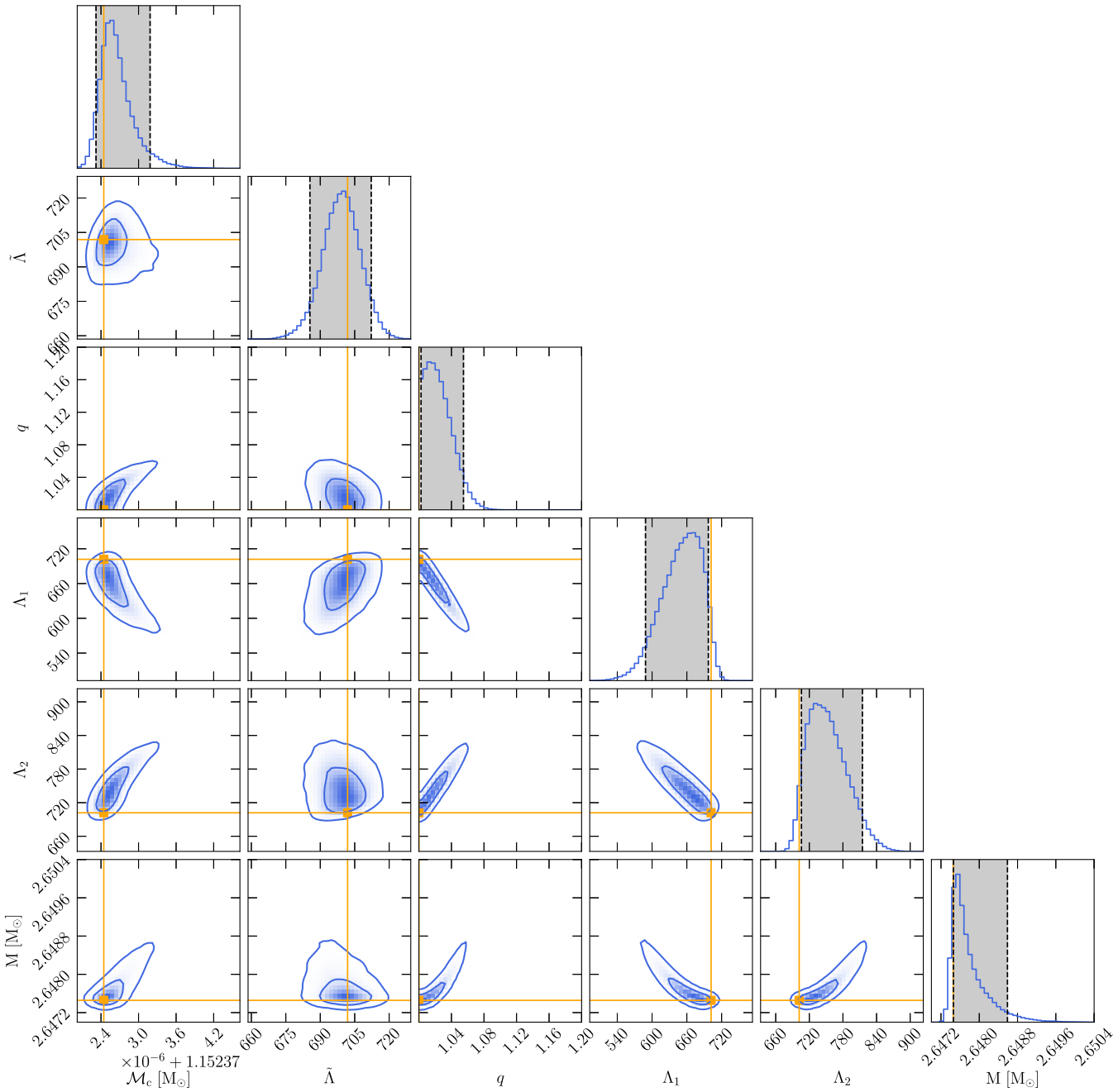

FIG. 17. Corner plot depicting the posteriors on chirp mass $\mathcal{M}_c$, tidal deformability $\tilde{\Lambda}$, mass ratio q, individual tidal parameters Λ_is and the total mass M for the binary $1.298M_\odot - 1.298M_\odot$ with the BLh EOS. The fact that the posteriors on mass ratio are one-sided influences the measurements of Λ_1, Λ_2, and M.

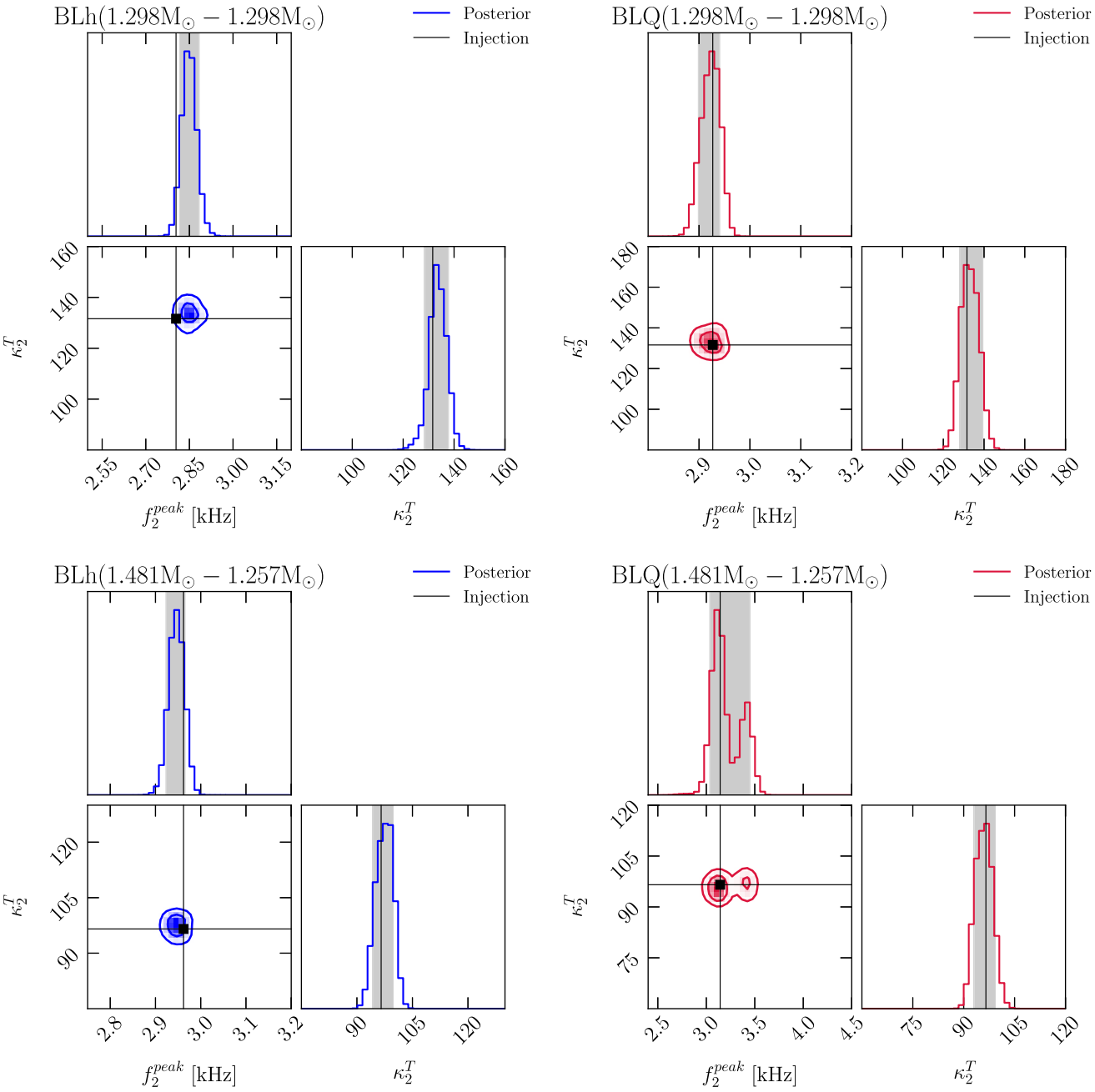

FIG. 18. Same calculations as in Fig. 6 for the binaries $1.298M_\odot - 1.298M_\odot$ and $1.481M_\odot - 1.257M_\odot$ with the BLh and BLQ EOSs. We note that the NRPMw model captures to within 90% CIs the f_2^{peak} frequency for the quark EOSs; however, the measurement of the same for hadronic model $1.298M_\odot - 1.298M_\odot$ suffers from a systematic bias that of multiple amplitude modulations. The double-peaked feature in the $1.481M_\odot - 1.257M_\odot$ binary is because this system is the shortest lived of all our simulations due to which the uncertainties in the measurement of postmerger frequency are the highest.

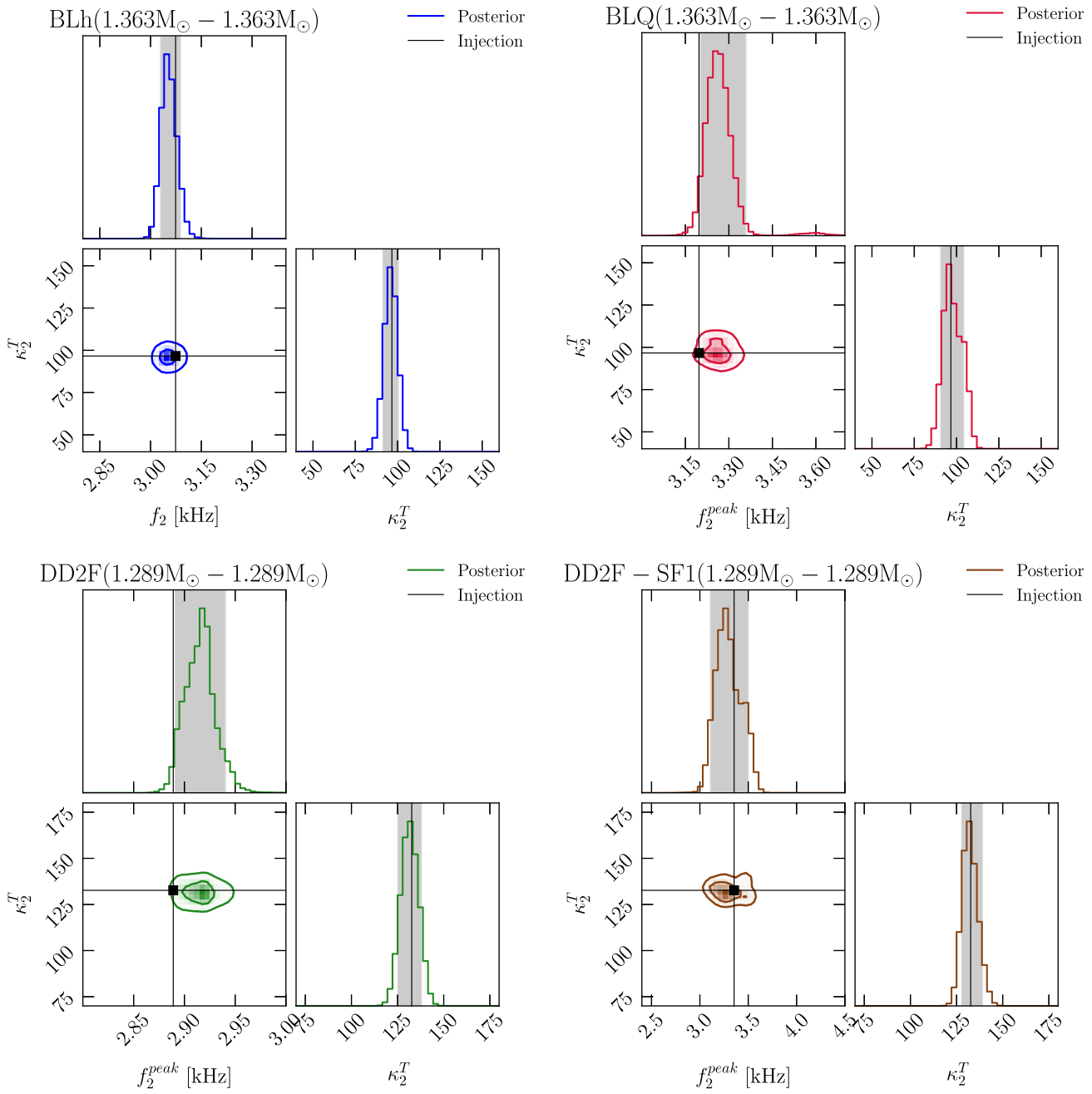

FIG. 19. Same calculations as in Fig. 6 for the binary $1.363M_\odot - 1.363M_\odot$ with the BLh and BLQ EOS and the binary $1.289M_\odot - 1.289M_\odot$ with the DD2F and DD2F-SF1 EOS.

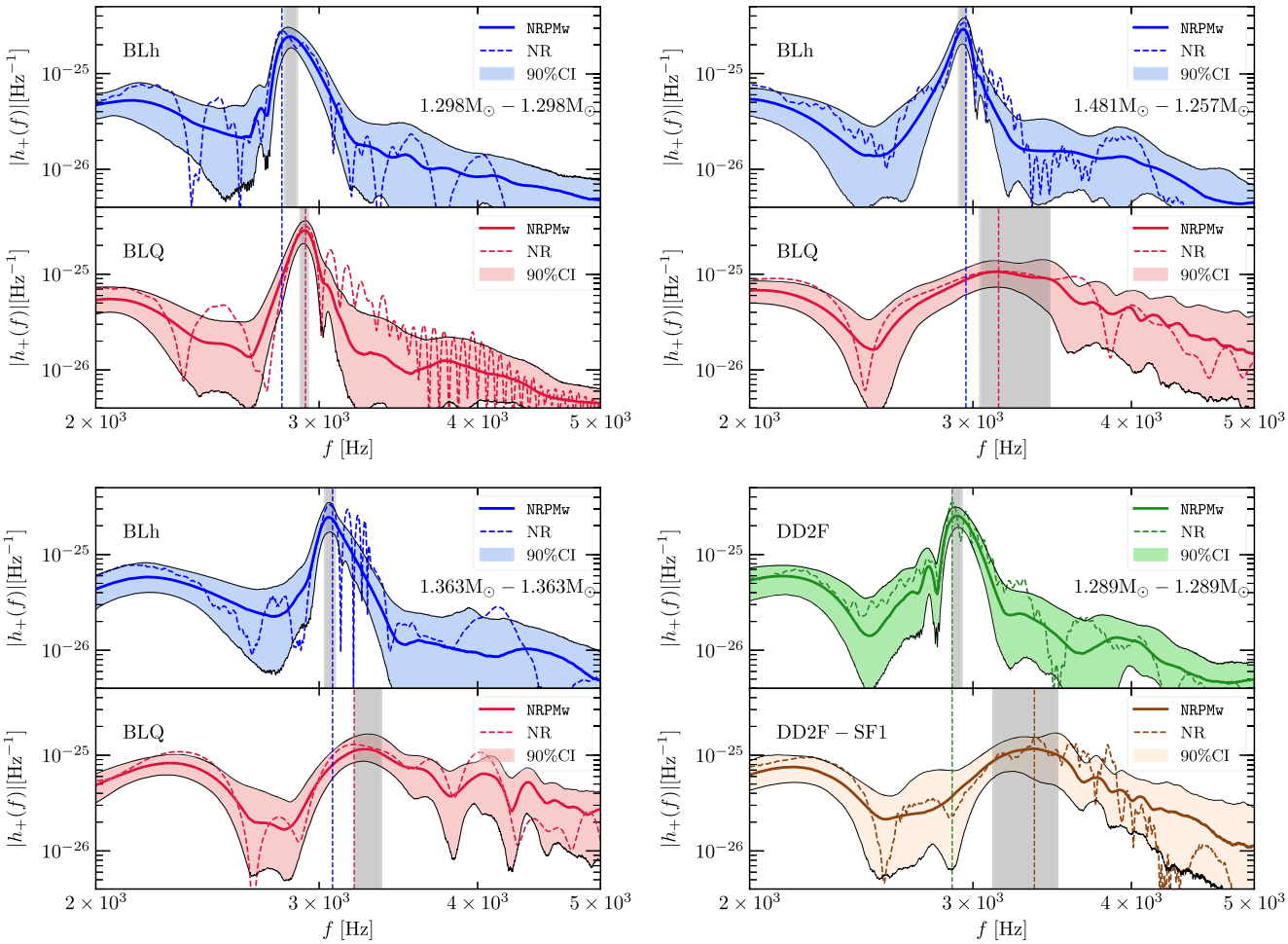

FIG. 20. Same calculation as in Fig. 7, i.e., reconstructed spectra for the binaries $1.298M_\odot - 1.298M_\odot$, $1.481M_\odot - 1.257M_\odot$, and $1.363M_\odot - 1.363M_\odot$ with the BLh and BLQ EOS as well as for the binary $1.289M_\odot - 1.289M_\odot$ with the DD2F and DD2F-SF1 EOS.

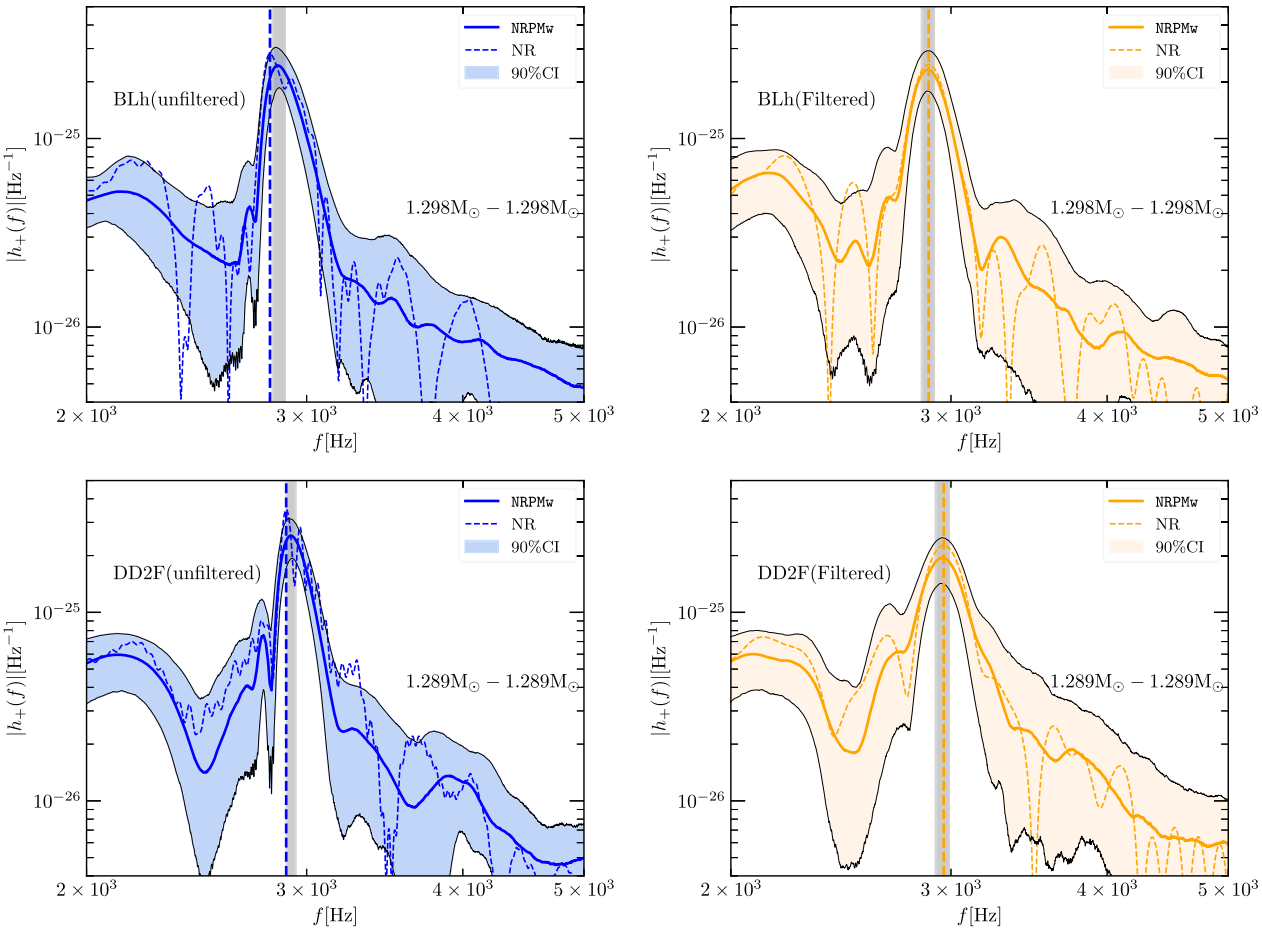

FIG. 21. Same calculations as in Fig. 8 for the binary $1.298M_\odot - 1.298M_\odot$ with the BLh EOS and the binary $1.289M_\odot - 1.289M_\odot$ with the DD2F EOS. Here, we show that the exclusion of more than two amplitude modulations in the strain can lead to recovery of the f_2^{peak} to within 90% CIs at a postmerger SNR of 10.

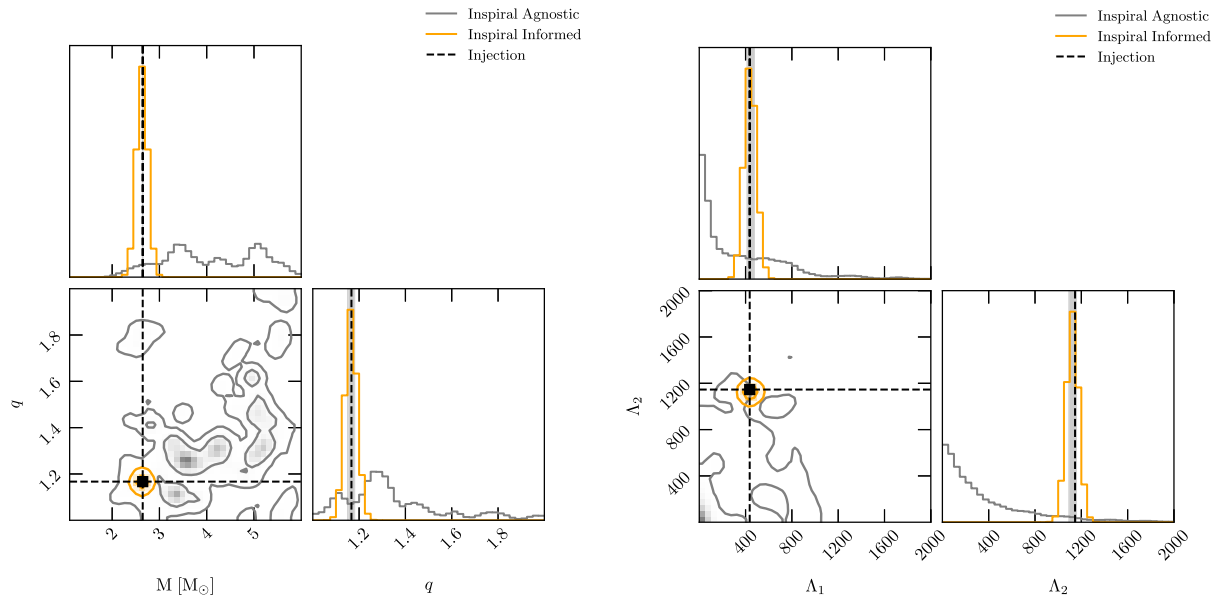

FIG. 22. Left panel: the posterior distributions of the total mass and mass ratio from a postmerger PE of the binary $1.398M_\odot - 1.198M_\odot$ with the BLh EOS compared between the two choice of priors used in this work. Right panel: the posterior PDFs for the component tidal deformabilities. In both cases we notice a clear improvement in accuracy for the measurement of M, q, Λ_1, and Λ_2.

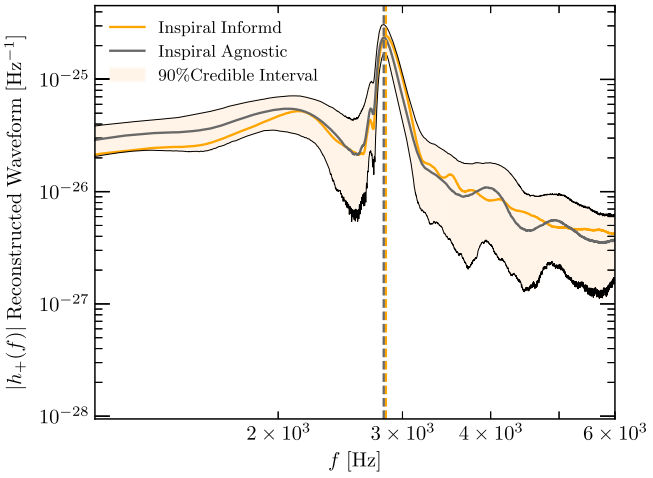

FIG. 23. The reconstructed NRPMw waveforms for a postmerger PE of the binary $1.398M_\odot - 1.198M_\odot$ with the BLh EOS corresponding to both the choices of priors. Both the reconstructions lie within the 90% CIs of each injection and the $f_2^{\rm peak}$ frequency shows only a miniscule deviation of ≈0.3%.

In Figs. 22 and 23, we show a comparison between posterior PDFs of the total mass M, mass ratio q and tidal parameters Λ_is between the cases of inspiral informed and inspiral agnostic priors. We note the significant improvement in the estimation of masses and tidal parameters upon including inspiral information, which is essentially a recovery of the priors that are informed of the inspiral signal. As we have stressed in the main text, we require reliable estimates of the inspiral signal to consistently probe QCD phase transitions from the EOS insensitive relations.

APPENDIX C: INFERENCE WITH UNCONSTRAINED f_2 AND f_0 PARAMETERS

In this appendix, we attempt to mitigate the source of bias in our hadronic models namely multiple amplitude modulations. We have seen in Sec. III A 1 that NRPMw can only capture the first two peaks of the postmerger amplitude modulations, which leads to an overestimation of the $f_2^{\rm peak}$ frequency. We test a new model configuration, in which we attempt to increase the flexibility of the model by freeing from universal relations not just the postmerger peak frequency parameter f_2, but also the parameter that models the radial pulsation modes of the remnant, i.e., f_0. We call this model configuration as NRPMw_v2 to distinguish from the other configurations employed in this work. This means that we do not use the recalibration parameter δf_0 that provided flexibility to the inference of f_0 when constrained from the universal relations instead, we set uniform priors on f_0 ranging between 0.1 to 2.5 kHz. The expectation is that making f_0 unconstrained can perhaps push the $\tilde{W}$pul wavelet that models amplitude modulations as defined in [68], to include more of the amplitude modulations.

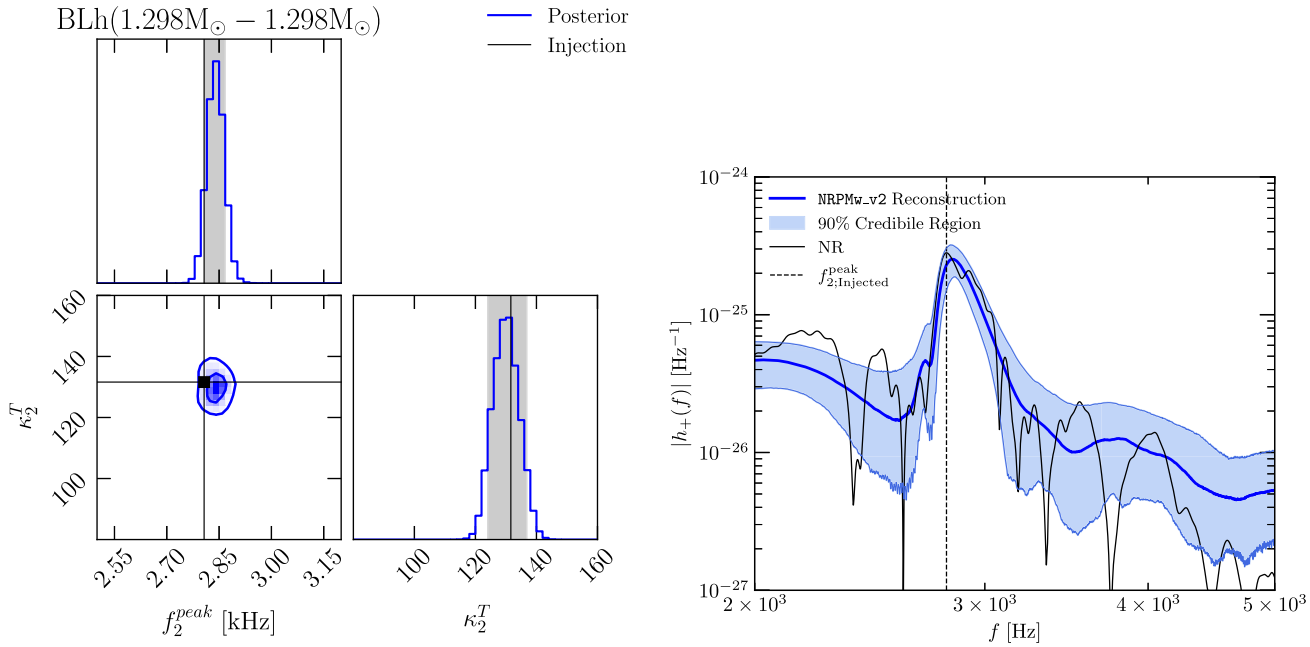

FIG. 24. Left panel: the posterior distributions of the postmerger peak frequency $f_2^{\rm peak}$ and the tidal polarizability κ_2^T corresponding to the $1.298M_\odot - 1.298M_\odot$ binary with the BLh EOS. Also shown is the lack of covariance of $f_2^{\rm peak}$ with κ_2^T owing to the corresponding QUR being not used. The contours correspond to the 50% and 90% CIs of the joint PDF. Right panel: the median reconstructed waveform from NRPMw_v2 shown along with the NR waveform.

We report however that this approach leads to only marginal improvements. We take the case of the $1.298M_\odot - 1.298M_\odot$ binary where the bias in measurement of $f_2^{\rm peak}$ is the largest. In Fig. 24, we report the same injection now being recovered from the modified NRPMw_v2 model configuration. We report that with the NRPMw model, 99.5% CIs of the $f_2^{\rm peak}$ posterior contained the injection, which is now marginally improved to 97% CIs containing the injection with NRPMw_v2. Nevertheless, the model configuration still reliably reconstructs the postmerger signal with a recovered SNR of 8.6 corresponding to an injected SNR of 10.

Finally, in Fig. 25, we show a comparison of the joint $f_2^{\rm peak} - \kappa_2^T$ posterior between the NRPMw and the NRPMw_v2 model configurations, with reference to the $f_2 - \kappa_2^T$ universal relation. For both the configurations, the 90% contours of the joint posterior capture the injection. We compute the Bayes' factor between the two models and find that $\log \mathcal{B}.\mathcal{F}^{\rm NRPMw}_{\rm NRPMw\_v2} = 0.06^{+0.28}_{-0.28}$ indicating that there is no preference to either models at a postmerger SNR of 10.

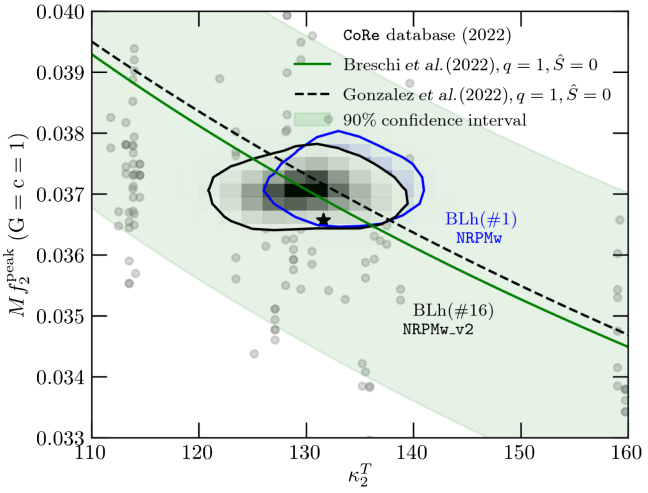

FIG. 25. A comparison of the joint $f_2^{\rm peak} - \kappa_2^T$ posterior for the $1.298M_\odot - 1.298M_\odot$ binary between the NRPMw and NRPMw_v2 model configurations. We see that the 90% contours of the joint posteriors for both the model configurations contain the injection.

[1] B. P. Abbott *et al.* (LIGO Scientific and Virgo Collaborations), GW170817: Observation of gravitational waves from a binary neutron star inspiral, Phys. Rev. Lett. **119**, 161101 (2017).

[2] B. P. Abbott *et al.* (LIGO Scientific, Virgo, Fermi GBM, INTEGRAL, IceCube, AstroSat Cadmium Zinc Telluride Imager Team, IPN, Insight-Hxmt, ANTARES, Swift, AGILE Team, 1M2H Team, Dark Energy Camera GW-EM, DES, DLT40, GRAWITA, Fermi-LAT, ATCA, ASKAP, Las Cumbres Observatory Group, OzGrav, DWF (Deeper Wider Faster Program), AST3, CAASTRO, VINROUGE, MASTER, J-GEM, GROWTH, JAGWAR, CaltechNRAO, TTU-NRAO, NuSTAR, Pan-STARRS, MAXI Team, TZAC Consortium, KU, Nordic Optical Telescope, ePESSTO, GROND, Texas Tech University, SALT Group, TOROS, BOOTES, MWA, CALET, IKI-GW Follow-up, H.E.S.S., LOFAR, LWA, HAWC, Pierre Auger, ALMA, Euro VLBI Team, Pi of Sky, Chandra Team at McGill University, DFN, ATLAS Telescopes, High Time Resolution Universe Survey, RIMAS, RATIR, and SKA South Africa/MeerKAT Collaborations), Multi-messenger observations of a binary neutron star merger, Astrophys. J. Lett. **848**, L12 (2017).

[3] D. Radice, S. Bernuzzi, and A. Perego, The dynamics of binary neutron star mergers and GW170817, Annu. Rev. Nucl. Part. Sci. **70**, 95 (2020).

[4] S. Bernuzzi, Neutron star merger remnants, Gen. Relativ. Gravit. **52**, 108 (2020).

[5] M. Punturo *et al.*, The Einstein Telescope: A third-generation gravitational wave observatory, Classical Quantum Gravity **27**, 194002 (2010).

[6] S. Hild *et al.*, Sensitivity studies for third-generation gravitational wave observatories, Classical Quantum Gravity **28**, 094013 (2011).

[7] B. P. Abbott *et al.* (LIGO Scientific Collaboration), Exploring the sensitivity of next generation gravitational wave detectors, Classical Quantum Gravity **34**, 044001 (2017).

[8] D. Reitze *et al.*, Cosmic Explorer: The U.S. contribution to gravitational-wave astronomy beyond LIGO, Bull. Am. Astron. Soc. **51**, 035 (2019), https://baas.aas.org/pub/2020n7i035/release/1.

[9] M. Evans *et al.*, A horizon study for Cosmic Explorer: Science, observatories, and community, arXiv:2109.09882.

[10] M. Evans *et al.*, Cosmic Explorer: A submission to the NSF MPSAC ngGW subcommittee, arXiv:2306.13745.

[11] M. Branchesi *et al.*, Science with the Einstein Telescope: A comparison of different designs, J. Cosmol. Astropart. Phys. 07 (2023) 068.

[12] I. Gupta *et al.*, Characterizing gravitational wave detector networks: From $A^\sharp$ to Cosmic Explorer, arXiv:2307.10421.

[13] A. Perego, S. Bernuzzi, and D. Radice, Thermodynamics conditions of matter in neutron star mergers, Eur. Phys. J. A **55**, 124 (2019).

[14] P. Hammond, I. Hawke, and N. Andersson, Thermal aspects of neutron star mergers, Phys. Rev. D **104**, 103006 (2021).

[15] S. Blacker, A. Bauswein, and S. Typel, Exploring thermal effects of the hadron-quark matter transition in neutron star mergers, Phys. Rev. D **108**, 063032 (2023).

[16] E. R. Most and C. A. Raithel, Impact of the nuclear symmetry energy on the post-merger phase of a binary

neutron star coalescence, Phys. Rev. D **104**, 124012 (2021).
[17] J. Fields, A. Prakash, M. Breschi, D. Radice, S. Bernuzzi, and A. d. S. Schneider, Thermal effects in binary neutron star mergers, Astrophys. J. Lett. **952**, L36 (2023).
[18] D. Radice, F. Galeazzi, J. Lippuner, L. F. Roberts, C. D. Ott, and L. Rezzolla, Dynamical mass ejection from binary neutron star mergers, Mon. Not. R. Astron. Soc. **460**, 3255 (2016).
[19] D. Radice, A. Perego, K. Hotokezaka, S. A. Fromm, S. Bernuzzi, and L. F. Roberts, Binary neutron star mergers: Mass ejection, electromagnetic counterparts and nucleosynthesis, Astrophys. J. **869**, 130 (2018).
[20] D. Radice, S. Bernuzzi, A. Perego, and R. Haas, A new moment-based general-relativistic neutrino-radiation transport code: Methods and first applications to neutron star mergers, Mon. Not. R. Astron. Soc. **512**, 1499 (2022).
[21] F. Schianchi, H. Gieg, V. Nedora, A. Neuweiler, M. Ujevic, M. Bulla, and T. Dietrich, M1 neutrino transport within the numerical-relativistic code BAM with application to low mass binary neutron star mergers, Phys. Rev. D **109**, 044012 (2024).
[22] F. Foucart, Neutrino transport in general relativistic neutron star merger simulations, Living Rev. Comput. Astrophys. **9**, 1 (2023).
[23] D. Radice and S. Bernuzzi, *Ab-initio* general-relativistic neutrino-radiation hydrodynamics simulations of long-lived neutron star merger remnants to neutrino cooling timescales, Astrophys. J. **959**, 46 (2023).
[24] F. Zappa, S. Bernuzzi, D. Radice, and A. Perego, Binary neutron star merger simulations with neutrino transport and turbulent viscosity: Impact of different schemes and grid resolution, Mon. Not. R. Astron. Soc. **520**, 1481 (2023).
[25] E. Loffredo, A. Perego, D. Logoteta, and M. Branchesi, Muons in the aftermath of neutron star mergers and their impact on trapped neutrinos, Astron. Astrophys. **672**, A124 (2023).
[26] A. Camilletti, L. Chiesa, G. Ricigliano, A. Perego, L. C. Lippold, S. Padamata, S. Bernuzzi, D. Radice, D. Logoteta, and F. M. Guercilena, Numerical relativity simulations of the neutron star merger GW190425: Microphysics and mass ratio effects, Mon. Not. R. Astron. Soc. **516**, 4760 (2023).
[27] E. R. Most, S. P. Harris, C. Plumberg, M. G. Alford, J. Noronha, J. Noronha-Hostler, F. Pretorius, H. Witek, and N. Yunes, Projecting the likely importance of weak-interaction-driven bulk viscosity in neutron star mergers, Mon. Not. R. Astron. Soc. **509**, 1096 (2021).
[28] E. R. Most, A. Haber, S. P. Harris, Z. Zhang, M. G. Alford, and J. Noronha, Emergence of microphysical viscosity in binary neutron star post-merger dynamics, arXiv:2207.00442.
[29] L. Combi and D. M. Siegel, GRMHD simulations of neutron-star mergers with weak interactions: r-process nucleosynthesis and electromagnetic signatures of dynamical ejecta, Astrophys. J. **944**, 28 (2023).
[30] M. George, M.-R. Wu, I. Tamborra, R. Ardevol-Pulpillo, and H.-T. Janka, Fast neutrino flavor conversion, ejecta properties, and nucleosynthesis in newly-formed hypermassive remnants of neutron-star mergers, Phys. Rev. D **102**, 103015 (2020).
[31] D. M. Siegel and B. D. Metzger, Three-dimensional GRMHD simulations of neutrino-cooled accretion disks from neutron star mergers, Astrophys. J. **858**, 52 (2018).
[32] D. Martin, A. Perego, W. Kastaun, and A. Arcones, The role of weak interactions in dynamic ejecta from binary neutron star mergers, Classical Quantum Gravity **35**, 034001 (2018).
[33] S. Fujibayashi, M. Shibata, S. Wanajo, K. Kiuchi, K. Kyutoku, and Y. Sekiguchi, Mass ejection from disks surrounding a low-mass black hole: Viscous neutrino-radiation hydrodynamics simulation in full general relativity, Phys. Rev. D **101**, 083029 (2020).
[34] E. Grohs, S. Richers, S. M. Couch, F. Foucart, J. P. Kneller, and G. C. McLaughlin, Neutrino fast flavor instability in three dimensions for a neutron star merger, Phys. Lett. B **846**, 138210 (2023).
[35] E. Grohs, S. Richers, S. M. Couch, F. Foucart, J. Froustey, J. Kneller, and G. McLaughlin, Two-moment neutrino flavor transformation with applications to the fast flavor instability in neutron star mergers, arXiv:2309.00972.
[36] S. A. Richers, G. C. McLaughlin, J. P. Kneller, and A. Vlasenko, Neutrino quantum kinetics in compact objects, Phys. Rev. D **99**, 123014 (2019).
[37] Y. Sekiguchi, K. Kiuchi, K. Kyutoku, and M. Shibata, Effects of hyperons in binary neutron star mergers, Phys. Rev. Lett. **107**, 211101 (2011).
[38] D. Radice, S. Bernuzzi, W. Del Pozzo, L. F. Roberts, and C. D. Ott, Probing extreme-density matter with gravitational wave observations of binary neutron star merger remnants, Astrophys. J. Lett. **842**, L10 (2017).
[39] E. R. Most, L. J. Papenfort, V. Dexheimer, M. Hanauske, S. Schramm, H. Stöcker, and L. Rezzolla, Signatures of quark-hadron phase transitions in general-relativistic neutron-star mergers, Phys. Rev. Lett. **122**, 061101 (2019).
[40] E. R. Most, L. Jens Papenfort, V. Dexheimer, M. Hanauske, H. Stoecker, and L. Rezzolla, On the deconfinement phase transition in neutron-star mergers, Eur. Phys. J. A **56**, 59 (2020).
[41] A. Bauswein, N.-U. F. Bastian, D. B. Blaschke, K. Chatziioannou, J. A. Clark, T. Fischer, and M. Oertel, Identifying a first-order phase transition in neutron star mergers through gravitational waves, Phys. Rev. Lett. **122**, 061102 (2019).
[42] A. Bauswein and S. Blacker, Impact of quark deconfinement in neutron star mergers and hybrid star mergers, Eur. Phys. J. Spec. Top. **229**, 3595 (2020).
[43] S. Blacker, N.-U. F. Bastian, A. Bauswein, D. B. Blaschke, T. Fischer, M. Oertel, T. Soultanis, and S. Typel, Constraining the onset density of the hadron-quark phase transition with gravitational-wave observations, Phys. Rev. D **102**, 123023 (2020).
[44] L. R. Weih, M. Hanauske, and L. Rezzolla, Postmerger gravitational-wave signatures of phase transitions in binary mergers, Phys. Rev. Lett. **124**, 171103 (2020).
[45] A. Prakash, D. Radice, D. Logoteta, A. Perego, V. Nedora, I. Bombaci, R. Kashyap, S. Bernuzzi, and A. Endrizzi, Signatures of deconfined quark phases in binary neutron star mergers, Phys. Rev. D **104**, 083029 (2021).

[46] S. L. Liebling, C. Palenzuela, and L. Lehner, Effects of high density phase transitions on neutron star dynamics, Classical Quantum Gravity **38**, 115007 (2021).
[47] A. Kedia, H. I. Kim, I.-S. Suh, and G. J. Mathews, Binary neutron star mergers as a probe of quark-hadron crossover equations of state, Phys. Rev. D **106**, 103027 (2022).
[48] G. J. Mathews, A. Kedia, H. I. Kim, and I.-S. Suh, Neutron star mergers and the quark matter equation of state, EPJ Web Conf. **274**, 01013 (2022).
[49] Y.-J. Huang, L. Baiotti, T. Kojo, K. Takami, H. Sotani, H. Togashi, T. Hatsuda, S. Nagataki, and Y.-Z. Fan, Merger and postmerger of binary neutron stars with a quark-hadron crossover equation of state, Phys. Rev. Lett. **129**, 181101 (2022).
[50] Y. Fujimoto, K. Fukushima, K. Hotokezaka, and K. Kyutoku, Gravitational wave signal for quark matter with realistic phase transition, Phys. Rev. Lett. **130**, 091404 (2023).
[51] S. Tootle, C. Ecker, K. Topolski, T. Demircik, M. Järvinen, and L. Rezzolla, Quark formation and phenomenology in binary neutron-star mergers using V-QCD, SciPost Phys. **13**, 109 (2022).
[52] T. Demircik, C. Ecker, M. Järvinen, L. Rezzolla, S. Tootle, and K. Topolski, Exploring the phase diagram of V-QCD with neutron star merger simulations, EPJ Web Conf. **274**, 07006 (2022).
[53] P. L. Espino, A. Prakash, D. Radice, and D. Logoteta, Revealing phase transition in dense matter with gravitational wave spectroscopy of binary neutron star mergers, arXiv:2301.03619.
[54] L.-J. Guo, W.-C. Yang, Y.-L. Ma, and Y.-L. Wu, Probing hadron-quark transition through binary neutron star merger, arXiv:2308.01770.
[55] S. Haque, R. Mallick, and S. K. Thakur, Binary neutron star mergers and the effect of onset of phase transition on gravitational wave signals, Mon. Not. R. Astron. Soc. **527**, 11575 (2024).
[56] R. Ciolfi, The key role of magnetic fields in binary neutron star mergers, Gen. Relativ. Gravit. **52**, 59 (2020).
[57] R. Ciolfi, W. Kastaun, B. Giacomazzo, A. Endrizzi, D. M. Siegel, and R. Perna, General relativistic magnetohydrodynamic simulations of binary neutron star mergers forming a long-lived neutron star, Phys. Rev. D **95**, 063016 (2017).
[58] D. Radice, General-relativistic large-eddy simulations of binary neutron star mergers, Astrophys. J. Lett. **838**, L2 (2017).
[59] M. Shibata and K. Kiuchi, Gravitational waves from remnant massive neutron stars of binary neutron star merger: Viscous hydrodynamics effects, Phys. Rev. D **95**, 123003 (2017).
[60] B. Margalit, A. S. Jermyn, B. D. Metzger, L. F. Roberts, and E. Quataert, Angular-momentum transport in proto-neutron stars and the fate of neutron star merger remnants, Astrophys. J. **939**, 51 (2022).
[61] K. Hotokezaka, K. Kiuchi, K. Kyutoku, T. Muranushi, Y.-i. Sekiguchi, M. Shibata, and K. Taniguchi, Remnant massive neutron stars of binary neutron star mergers: Evolution process and gravitational waveform, Phys. Rev. D **88**, 044026 (2013).
[62] A. Bauswein, N. Stergioulas, and H.-T. Janka, Exploring properties of high-density matter through remnants of neutron-star mergers, Eur. Phys. J. A **52**, 56 (2016).
[63] S. Bose, K. Chakravarti, L. Rezzolla, B. S. Sathyaprakash, and K. Takami, Neutron-star radius from a population of binary neutron star mergers, Phys. Rev. Lett. **120**, 031102 (2018).
[64] P. J. Easter, S. Ghonge, P. D. Lasky, A. R. Casey, J. A. Clark, F. H. Vivanco, and K. Chatziioannou, Detection and parameter estimation of binary neutron star merger remnants, Phys. Rev. D **102**, 043011 (2020).
[65] T. Soultanis, A. Bauswein, and N. Stergioulas, Analytic models of the spectral properties of gravitational waves from neutron star merger remnants, Phys. Rev. D **105**, 043020 (2022).
[66] K. W. Tsang, T. Dietrich, and C. Van Den Broeck, Modeling the postmerger gravitational wave signal and extracting binary properties from future binary neutron star detections, Phys. Rev. D **100**, 044047 (2019).
[67] M. Breschi, S. Bernuzzi, F. Zappa, M. Agathos, A. Perego, D. Radice, and A. Nagar, kiloHertz gravitational waves from binary neutron star remnants: Time-domain model and constraints on extreme matter, Phys. Rev. D **100**, 104029 (2019).
[68] M. Breschi, S. Bernuzzi, K. Chakravarti, A. Camilletti, A. Prakash, and A. Perego, Kilohertz gravitational waves from binary neutron star mergers: Numerical-relativity informed postmerger model, arXiv:2205.09112.
[69] K. Chatziioannou, J. A. Clark, A. Bauswein, M. Millhouse, T. B. Littenberg, and N. Cornish, Inferring the post-merger gravitational wave emission from binary neutron star coalescences, Phys. Rev. D **96**, 124035 (2017).
[70] M. Wijngaarden, K. Chatziioannou, A. Bauswein, J. A. Clark, and N. J. Cornish, Probing neutron stars with the full premerger and postmerger gravitational wave signal from binary coalescences, Phys. Rev. D **105**, 104019 (2022).
[71] M. Breschi, R. Gamba, S. Borhanian, G. Carullo, and S. Bernuzzi, Kilohertz gravitational waves from binary neutron star mergers: Inference of postmerger signals with the Einstein Telescope, arXiv:2205.09979.
[72] M. Breschi, G. Carullo, and S. Bernuzzi, Pre/post-merger consistency test for gravitational signals from binary neutron star mergers, arXiv:2301.09672.
[73] R. Harada, K. Cannon, K. Hotokezaka, and K. Kyutoku, On the testability of the quark-hadron transition using gravitational waves from merging binary neutron stars, arXiv:2310.13603.
[74] S. Han and A. W. Steiner, Tidal deformability with sharp phase transitions in (binary) neutron stars, Phys. Rev. D **99**, 083014 (2019).
[75] M. Sieniawska, W. Turczanski, M. Bejger, and J. L. Zdunik, Tidal deformability and other global parameters of compact stars with strong phase transitions, Astron. Astrophys. **622**, A174 (2019).
[76] C. A. Raithel and E. R. Most, Degeneracy in the inference of phase transitions in the neutron star equation of state from gravitational wave data, Phys. Rev. Lett. **130**, 201403 (2023).

[77] R. Essick, I. Legred, K. Chatziioannou, S. Han, and P. Landry, Phase transition phenomenology with nonparametric representations of the neutron star equation of state, Phys. Rev. D **108**, 043013 (2023).
[78] C. Mondal, M. Antonelli, F. Gulminelli, M. Mancini, J. Novak, and M. Oertel, Detectability of a phase transition in neutron star matter with third-generation gravitational wave interferometers, Mon. Not. R. Astron. Soc. **524**, 3464 (2023).
[79] C. A. Raithel and E. R. Most, Tidal deformability Doppelgänger: Implications of a low-density phase transition in the neutron star equation of state, Phys. Rev. D **108**, 023010 (2023).
[80] P. T. H. Pang, T. Dietrich, I. Tews, and C. Van Den Broeck, Parameter estimation for strong phase transitions in supranuclear matter using gravitational-wave astronomy, Phys. Rev. Res. **2**, 033514 (2020).
[81] A. Bauswein and H. T. Janka, Measuring neutron-star properties via gravitational waves from binary mergers, Phys. Rev. Lett. **108**, 011101 (2012).
[82] S. Bernuzzi, A. Nagar, S. Balmelli, T. Dietrich, and M. Ujevic, Quasiuniversal properties of neutron star mergers, Phys. Rev. Lett. **112**, 201101 (2014).
[83] S. Bernuzzi, T. Dietrich, and A. Nagar, Modeling the complete gravitational wave spectrum of neutron star mergers, Phys. Rev. Lett. **115**, 091101 (2015).
[84] L. Rezzolla and K. Takami, Gravitational-wave signal from binary neutron stars: A systematic analysis of the spectral properties, Phys. Rev. D **93**, 124051 (2016).
[85] F. Zappa, S. Bernuzzi, D. Radice, A. Perego, and T. Dietrich, Gravitational-wave luminosity of binary neutron stars mergers, Phys. Rev. Lett. **120**, 111101 (2018).
[86] A. Bauswein, H. T. Janka, K. Hebeler, and A. Schwenk, Equation-of-state dependence of the gravitational-wave signal from the ring-down phase of neutron-star mergers, Phys. Rev. D **86**, 063001 (2012).
[87] G. Lioutas, A. Bauswein, and N. Stergioulas, Frequency deviations in universal relations of isolated neutron stars and postmerger remnants, Phys. Rev. D **104**, 043011 (2021).
[88] S. Typel, G. Ropke, T. Klahn, D. Blaschke, and H. H. Wolter, Composition and thermodynamics of nuclear matter with light clusters, Phys. Rev. C **81**, 015803 (2010).
[89] D. Alvarez-Castillo, A. Ayriyan, S. Benic, D. Blaschke, H. Grigorian, and S. Typel, New class of hybrid EoS and Bayesian M-R data analysis, Eur. Phys. J. A **52**, 69 (2016).
[90] T. Fischer, N.-U. F. Bastian, M.-R. Wu, P. Baklanov, E. Sorokina, S. Blinnikov, S. Typel, T. Klähn, and D. B. Blaschke, Quark deconfinement as a supernova explosion engine for massive blue supergiant stars, Nat. Astron. **2**, 980 (2018).
[91] F. Banyuls, J. A. Font, J. M. A. Ibanez, J. M. A. Marti, and J. A. Miralles, Numerical $3+1$ general relativistic hydrodynamics: A local characteristic approach, Astrophys. J. **476**, 221 (1997).
[92] D. Radice and L. Rezzolla, THC: A new high-order finite-difference high-resolution shock-capturing code for special-relativistic hydrodynamics, Astron. Astrophys. **547**, A26 (2012).
[93] D. Radice, L. Rezzolla, and F. Galeazzi, Beyond second-order convergence in simulations of binary neutron stars in full general-relativity, Mon. Not. R. Astron. Soc. **437**, L46 (2014).
[94] D. Radice, L. Rezzolla, and F. Galeazzi, High-order fully general-relativistic hydrodynamics: New approaches and tests, Classical Quantum Gravity **31**, 075012 (2014).
[95] D. Pollney, C. Reisswig, E. Schnetter, N. Dorband, and P. Diener, High accuracy binary black hole simulations with an extended wave zone, Phys. Rev. D **83**, 044045 (2011).
[96] C. Reisswig, C. D. Ott, E. Abdikamalov, R. Haas, P. Moesta, and E. Schnetter, Formation and coalescence of cosmological supermassive black hole binaries in supermassive star collapse, Phys. Rev. Lett. **111**, 151101 (2013).
[97] L. Werneck *et al.*, The Einstein Toolkit, to find out more, visit http://einsteintoolkit.org (2023).
[98] S. Bernuzzi and D. Hilditch, Constraint violation in free evolution schemes: Comparing BSSNOK with a conformal decomposition of Z4, Phys. Rev. D **81**, 084003 (2010).
[99] D. Hilditch, S. Bernuzzi, M. Thierfelder, Z. Cao, W. Tichy, and B. Bruegmann, Compact binary evolutions with the Z4c formulation, Phys. Rev. D **88**, 084057 (2013).
[100] E. Gourgoulhon, P. Grandclement, K. Taniguchi, J.-A. Marck, and S. Bonazzola, Quasiequilibrium sequences of synchronized and irrotational binary neutron stars in general relativity: 1. Method and tests, Phys. Rev. D **63**, 064029 (2001).
[101] E. Schnetter, S. H. Hawley, and I. Hawke, Evolutions in 3-D numerical relativity using fixed mesh refinement, Classical Quantum Gravity **21**, 1465 (2004).
[102] C. Reisswig, R. Haas, C. D. Ott, E. Abdikamalov, P. Mösta, D. Pollney, and E. Schnetter, Three-dimensional general-relativistic hydrodynamic simulations of binary neutron star coalescence and stellar collapse with multipatch grids, Phys. Rev. D **87**, 064023 (2013).
[103] I. Bombaci and D. Logoteta, Equation of state of dense nuclear matter and neutron star structure from nuclear chiral interactions, Astron. Astrophys. **609**, A128 (2018).
[104] D. Logoteta, A. Perego, and I. Bombaci, Microscopic equation of state of hot nuclear matter for numerical relativity simulations, Astron. Astrophys. **646**, A55 (2021).
[105] R. Kashyap *et al.*, Numerical relativity simulations of prompt collapse mergers: Threshold mass and phenomenological constraints on neutron star properties after GW170817, Phys. Rev. D **105**, 103022 (2022).
[106] A. Perego, D. Logoteta, D. Radice, S. Bernuzzi, R. Kashyap, A. Das, S. Padamata, and A. Prakash, Probing the incompressibility of nuclear matter at ultrahigh density through the prompt collapse of asymmetric neutron star binaries, Phys. Rev. Lett. **129**, 032701 (2022).
[107] C. Reisswig and D. Pollney, Notes on the integration of numerical relativity waveforms, Classical Quantum Gravity **28**, 195015 (2011).
[108] S. Bernuzzi *et al.*, Accretion-induced prompt black hole formation in asymmetric neutron star mergers, dynamical ejecta and kilonova signals, Mon. Not. R. Astron. Soc. **497**, 1488 (2020).

[109] H. Bandyopadhyay, D. Radice, A. Prakash, A. Dhani, D. Logoteta, A. Perego, and R. Kashyap, Do black holes remember what they are made of?, arXiv:2312.11620.
[110] F. Harris, On the use of windows for harmonic analysis with the discrete Fourier transform, Proc. IEEE **66**, 51 (1978).
[111] J. Buchner, UltraNest—A robust, general purpose Bayesian inference engine, J. Open Source Softw. **6**, 3001 (2021).
[112] M. Breschi, R. Gamba, and S. Bernuzzi, Bayesian inference of multimessenger astrophysical data: Methods and applications to gravitational waves, Phys. Rev. D **104**, 042001 (2021).
[113] E. Thrane and C. Talbot, An introduction to Bayesian inference in gravitational-wave astronomy: Parameter estimation, model selection, and hierarchical models, Publ. Astron. Soc. Aust. **36**, e010 (2019); **37**, e036(E) (2020).
[114] T. Callister, A thesaurus for common priors in gravitational-wave astronomy, arXiv:2104.09508.
[115] B. S. Sathyaprakash and S. V. Dhurandhar, Choice of filters for the detection of gravitational waves from coalescing binaries, Phys. Rev. D **44**, 3819 (1991).
[116] A. Bohé, S. Marsat, and L. Blanchet, Next-to-next-to-leading order spin–orbit effects in the gravitational wave flux and orbital phasing of compact binaries, Classical Quantum Gravity **30**, 135009 (2013).
[117] K. G. Arun, A. Buonanno, G. Faye, and E. Ochsner, Higher-order spin effects in the amplitude and phase of gravitational waveforms emitted by inspiraling compact binaries: Ready-to-use gravitational waveforms, Phys. Rev. D **79**, 104023 (2009); **84**, 049901(E) (2011).
[118] B. Mikoczi, M. Vasuth, and L. A. Gergely, Self-interaction spin effects in inspiralling compact binaries, Phys. Rev. D **71**, 124043 (2005).
[119] A. Bohé, G. Faye, S. Marsat, and E. K. Porter, Quadratic-in-spin effects in the orbital dynamics and gravitational-wave energy flux of compact binaries at the 3PN order, Classical Quantum Gravity **32**, 195010 (2015).
[120] C. K. Mishra, A. Kela, K. G. Arun, and G. Faye, Ready-to-use post-Newtonian gravitational waveforms for binary black holes with nonprecessing spins: An update, Phys. Rev. D **93**, 084054 (2016).
[121] E. Poisson, Gravitational waves from inspiraling compact binaries: The Quadrupole moment term, Phys. Rev. D **57**, 5287 (1998).
[122] L. Wade, J. D. E. Creighton, E. Ochsner, B. D. Lackey, B. F. Farr, T. B. Littenberg, and V. Raymond, Systematic and statistical errors in a Bayesian approach to the estimation of the neutron-star equation of state using advanced gravitational wave detectors, Phys. Rev. D **89**, 103012 (2014).
[123] G. Ashton *et al.*, Bilby: A user-friendly Bayesian inference library for gravitational-wave astronomy, Astrophys. J. Suppl. Ser. **241**, 27 (2019).
[124] I. M. Romero-Shaw *et al.*, Bayesian inference for compact binary coalescences with Bilby: Validation and application to the first LIGO–Virgo gravitational-wave transient catalogue, Mon. Not. R. Astron. Soc. **499**, 3295 (2020).
[125] G. Ashton and C. Talbot, Bilby-MCMC: An MCMC sampler for gravitational-wave inference, Mon. Not. R. Astron. Soc. **507**, 2037 (2021).
[126] B. Zackay, L. Dai, and T. Venumadhav, Relative binning and fast likelihood evaluation for gravitational wave parameter estimation, arXiv:1806.08792.
[127] K. Krishna, A. Vijaykumar, A. Ganguly, C. Talbot, S. Biscoveanu, R. N. George, N. Williams, and A. Zimmerman, Accelerated parameter estimation in Bilby with relative binning, arXiv:2312.06009.
[128] K. Chatziioannou, C.-J. Haster, and A. Zimmerman, Measuring the neutron star tidal deformability with equation-of-state-independent relations and gravitational waves, Phys. Rev. D **97**, 104036 (2018).
[129] W. Kastaun and F. Ohme, Finite tidal effects in GW170817: Observational evidence or model assumptions?, Phys. Rev. D **100**, 103023 (2019).
[130] A. Gonzalez *et al.*, Second release of the CoRe database of binary neutron star merger waveforms, Classical Quantum Gravity **40**, 085011 (2023).
[131] A. Bauswein, S. Blacker, V. Vijayan, N. Stergioulas, K. Chatziioannou, J. A. Clark, N.-U. F. Bastian, D. B. Blaschke, M. Cierniak, and T. Fischer, Equation of state constraints from the threshold binary mass for prompt collapse of neutron star mergers, Phys. Rev. Lett. **125**, 141103 (2020).
[132] M. Aparicio Resco, A. de la Cruz-Dombriz, F. J. Llanes Estrada, and V. Zapatero Castrillo, On neutron stars in $f(R)$ theories: Small radii, large masses and large energy emitted in a merger, Phys. Dark Universe **13**, 147 (2016).
[133] E. Lope-Oter and A. Wojnar, Constraining Palatini gravity with GR-independent equations of state for neutron stars, J. Cosmol. Astropart. Phys. 02 (2024) 017.
[134] D. D. Doneva, C. J. Krüger, K. V. Staykov, and P. Y. Yordanov, Neutron stars in Gauss-Bonnet gravity: Nonlinear scalarization and gravitational phase transitions, Phys. Rev. D **108**, 044054 (2023).
[135] E. Lope-Oter and F. J. Llanes-Estrada, Maximum latent heat of neutron star matter independently of general relativity, Phys. Rev. C **105**, L052801 (2022).
[136] P. L. Espino, G. Bozzola, and V. Paschalidis, Quantifying uncertainties in general relativistic magnetohydrodynamic codes, Phys. Rev. D **107**, 104059 (2023).